Angular distributions of ejected electrons from autoionizing 3*pnd* states of magnesium

M. D. Lindsay, C.-J. Dai, L.-T. Cai, and T. F. Gallagher
Department of Physics, University of Virginia, Charlottesville, Virginia 22901

F. Robicheaux and C. H. Greene
Joint Institute for Laboratory Astrophysics and Department of Physics, University of Colorado, Boulder, Colorado 80309

(Received 23 December 1991; revised manuscript received 2 June 1992)

We have measured the angular distributions of electrons ejected from doubly excited autoionizing Rydberg $3pnd\ J=1$ and 3 states of magnesium, where $n=10-18$. To excite the aligned $3snd\ ^1D_2$ states of Mg, we used two dye lasers crossed with an atomic beam. A third laser, linearly polarized in the same direction as the other two, excited the atoms in the $3snd$ states to the $3pnd$ states. The angular distributions of ejected electrons are given by $d\sigma/d\Omega=\sum_k a_k P_k(\cos\theta)$, where $k=0,2,4,6$. We measured the angular distribution parameters a_k as a function of the energy of the third laser photon using an electron detector and a Mg^+ ion detector. We compare our results with the predictions of an R-matrix multichannel quantum-defect theory. We find good agreement between experiment and theory.

PACS number(s): 34.50.Lf, 32.80.Rm, 32.80.Dz, 82.50.Fv

I. INTRODUCTION

The R-matrix method, when combined with multichannel quantum-defect theory (MQDT) [1], has been used with extraordinary success in predicting the photoabsorption cross sections of alkaline-earth atoms in the energy range up to about 5 eV above the lowest ionization limit; an energy range that includes autoionizing states converging to low-lying excited states of the ion. The calculated photoabsorption spectra agree with both the vacuum-ultraviolet spectra from the ground-state and isolated-core-excitation spectra from bound Rydberg states [2–17]. A more stringent test of the calculations is to measure the angular distributions of the ejected electrons from autoionizing states, and several comparisons of this sort have been made [3–5,7,8,10–19], all between measured and calculated angular distributions of electrons resulting from the excitation of bound Rydberg $msns\ ^1S_0$ states to autoionizing $mpns\ J=1$ states. The agreement for angular distributions is reasonably good, but not as good as in the case of the photoabsorption spectra. A review of experimental and theoretical work done up to 1988 may be found in Ref. [20].

Here we report the measurements of the angular distributions of electrons ejected from Mg $3pnd$ autoionizing states. Using two lasers linearly polarized in the same direction, an aligned sample of Mg $3snd\ ^1D_2$ atoms is produced. These atoms are further excited by a laser linearly polarized in the same direction to the $3pnd\ J=1$ and 3 autoionizing states. In this case the Mg^+ ion is left in the $3s_{1/2}$ state and the departing electron can be in either the ϵp_j or ϵf_j continuum. This paper reports measurements and theoretical predictions in Mg of the higher-order angular distributions achieved by exciting an aligned, nonspherically symmetric Rydberg state to autoionizing states. The measured angular distributions are compared to those calculated using the $J=1$ and 3 $\underline{K}$ matrices, which give an excellent representation of the photoabsorption spectrum. As we shall see, the agreement between theory and experiment is good, but not quite as good as in the case of the photoabsorption line shape. These measurements provide useful insight into the validity of important MQDT calculations of other properties of Mg, such as its dielectronic recombination rate in a plasma [21].

In the following sections of the paper we present our experimental method, the theory, the experimental and theoretical results, and a discussion of the results. The Appendix contains an independently derived, alternative formulation of the theory.

II. EXPERIMENTAL METHOD

Our excitation scheme is shown in Fig. 1. The first laser photon excited one electron from the Mg ground state to the lowest excited state: $3s3s\ ^1S_0 \rightarrow 3s3p\ ^1P_1$. The second photon excited the same electron to a bound $3snd\ ^1D_2$ Rydberg state just below the ionization potential. Both photons were linearly polarized in the same direction, producing $m=0$ levels, where m is the azimuthal orbital angular momentum quantum number. The wavelength of the second laser was tuned over a range 375–400 nm to produce various n levels $n=10-18$ of the Rydberg d state. The energies of the $3snd\ ^1D_2$ states are given in Ref. [22]. The first two lasers were used solely to produce the aligned $3snd\ ^1D_2$ state. These lasers were fixed in frequency while measuring spectra of the autoionizing $3pnd$ states. The third and last linearly polarized photon excited the inner electron transition $3snd \rightarrow 3pnd$, producing the autoionizing state [23]. To conform to conventional descriptions we shall call the $3snd$ state $|J_0\rangle$; its total angular momentum is $J_0=2$. The autoionizing $3pnd$ state has $J=1$ or 3. The $3pnd$ levels converge to the two $3p$ Mg^+ ion levels that have a

fine-structure splitting of 92 cm^{-1}. Due to the finite widths of the 3*pnd* levels and the small Mg^+ 3*p* fine-structure interval, transitions to 3*pnd* levels converging to both $3p_{1/2}$ and $3p_{3/2}$ limits overlap and the third photon excites both of them. The transitions to $J=1$ and 3 levels overlap also. We tuned the third laser over a range of ~ 300 cm^{-1} centered on the ionic $3s_{1/2} \rightarrow 3p_{1/2}$ and $3p_{3/2}$ transitions, and measured the angular distributions of the ejected electrons as described below.

Each photon came from a dye-laser oscillator and amplifier, the output of which was doubled in an angle-tuned potassium dihydrogen phosphate crystal. A tracking device maintained the phase-matching angle of the third laser's doubling crystal as the third laser was tuned. The dye lasers were pumped by a pulsed neodymium-doped yttrium aluminum garnet (Nd:YAG) laser operating at a 20-Hz repetition rate. Each laser pulse had a pulse length of about 5 ns and a frequency width of about 1 cm^{-1}. The collinear laser beams crossed a thermal atomic beam of Mg at right angles. A diagram of our optical apparatus and detectors can be found in Fig. 2.

The first and second lasers entered the vacuum chamber from the left side of Fig. 2. Both passed through a uv-grade double Fresnel rhomb and linear polarizer to ensure that they were highly linearly polarized in the same direction. The double Fresnel rhomb functioned as an achromatic half-wave plate, allowing the initial polarization of the lasers to be rotated to any angle without loss of intensity. The linear polarizer after the rhomb was rotated to pass the rhomb's output and to ensure that the purity of the linear polarization was at least 100:1.

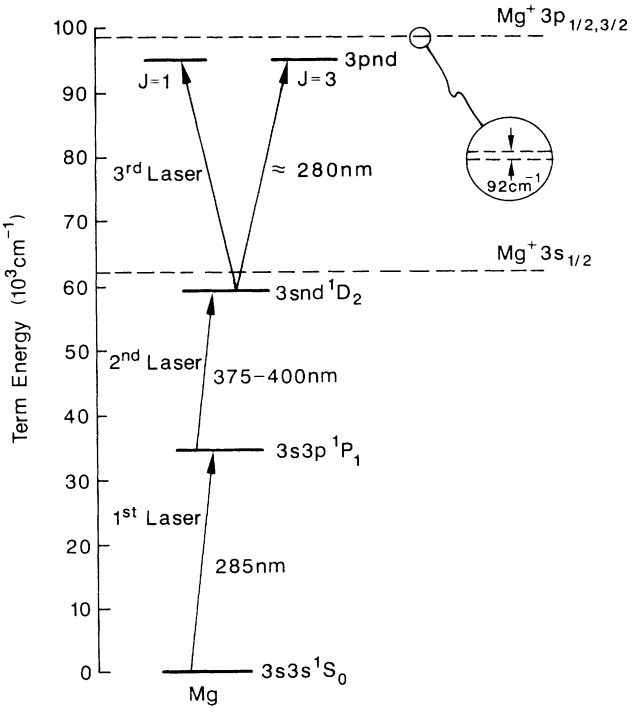

FIG. 1. Energy-level diagram for the three laser excitation of the 3*pnd* states of Mg. The first laser is fixed in frequency and excites the "outer" electron. The second laser excites the outer electron to a Rydberg state, with a particular *n* value in the range 10–18. The third laser excites the "inner" electron, and is tuned over a several-hundred-cm^{-1}-wide region centered on the autoionizing 3*pnd* resonances. All of the lasers are linearly polarized in the same direction. The angular distribution and line shape of the third transition are measured as a function of the tuning of the third laser. The 3*pnd* states are split by the 92 cm^{-1} fine-structure splitting of the excited ion core.

The third laser beam entered the vacuum chamber from the right side of Fig. 2, collinear to the first two. It passed through a similar polarization controller. The polarizations of all of the laser beams were always set to point in the same direction as the angle was varied. We found that the vacuum chamber windows had no effect on the laser polarization direction or purity.

A portion of the undoubled third laser beam was split off and sent into an Ar optogalvanic cell, which provided absolute frequency reference markers [24]. Another portion was sent through an étalon, providing fringes 4 cm^{-1} apart. These two signals were recorded simultaneously with all of our Mg spectra, giving us an absolute frequency calibration and a means of linearizing the scan of the third laser.

Our detectors, shown schematically in perspective in Fig. 2, consisted of an ion detector and an electron detector, each directly above or below the laser–atomic-beam interaction point. The line through this point and the detectors was perpendicular to the plane of the laser beams and atomic beam to within two degrees. Each detector was made of a stacked pair of microchannel plates (MCP's) biased with 2000 V of the appropriate polarity to detect positive ions or electrons. The MCP's were mounted at the back of a 10-cm-long tube to provide energy analysis and angular resolution for the electron detector. The negative high voltage at the face of the ion detector was completely shielded from the laser–atomic-beam interaction point by two grounded grids. A pair of grids parallel to the laser and atomic beams surrounded the laser–atomic-beam interaction point. These grids were kept grounded during the laser pulses. After about 1 μs, a brief high-voltage pulse was applied to force the entire slow-moving cloud of Mg^+ ions resulting from autoionization of the Mg 3*pnd* atoms to the ion detector. By the time the ion extraction pulse was applied, the electrons had already hit their detector. Time-of-flight energy analysis of the electron signal was necessary since the Mg atoms could be photoionized by absorbing two 285-nm photons from the first laser alone. This produced relatively low-energy photoelectrons, which arrived at the detector about 20 ns after the high-energy electrons emitted from the autoionizing 3*pnd* Mg states appeared at the detector. The electron pulses were only 2 or 3 ns long, so we could easily temporally resolve the two signals. The second electron pulse, having nothing to do with the 3*pnd* states, was eliminated entirely by using a gated integrator, which closed well before the second pulse arrived.

The electronics used to process the signals were the same as those described in detail in Ref. [19]. In brief, the MCP's amplified the electrons or ions by about 10^8. A separate fast amplifier brought the signals up to the

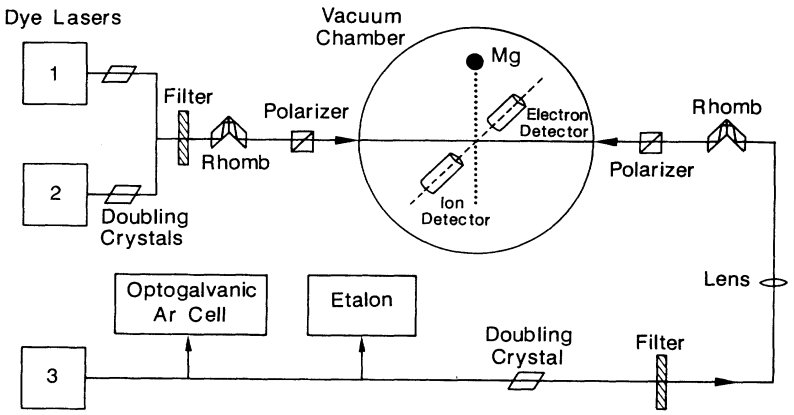

FIG. 2. Schematic diagram of the optical apparatus and detectors. The pump laser is not shown. Each dye laser is a combination of oscillator and amplifier. The doubling crystals are angle tuned; the crystal for the third laser is mounted in a servofeedback loop so that it tracks the tuning of the third laser. The filters block visible and ir light and only pass uv light. The optogalvanic Ar cell provides absolute frequency reference markers for the third laser. The étalon provides regularly spaced fringes for linearizing the scan of the third laser. Both the Ar cell and the étalon use undoubled light. The double Fresnel rhombs function as nearly achromatic half-wave plates to rotate the linear polarization of the lasers, allowing the detectors to measure different points in the angular distributions. The axis of rotation of the rhombs are the collinear laser beams themselves. The linear polarizers ensure that the laser beams are, in fact, linearly polarized. Each is rotated to match the setting of its rhomb. Each combination of rhomb and linear polarizer was always set to pass the direction of polarization as the other combination. The detectors are shown in perspective and are perpendicular to the plane of the drawing.

1 V level as soon as they exited the vacuum chamber. Gated integrators triggered by the laser pulses converted the signals to slowly varying dc levels. The gate width and delay were much greater for the ion pulses than for the electron pulses, since the ions traveled more slowly to their detector. An analog-to-digital converter and computer measured and recorded the electron and ion dc signals along with the Ar optogalvanic lines and étalon fringes for further analysis. To minimize distortions of the angular distributions, the entire region surrounding the path of the autoionized electrons was sprayed with graphite powder to reduce stray electric fields and was enclosed with two layers of μ metal to reduce stray magnetic fields.

The specific autoionizing Rydberg states we measured are $3pnd$, excited by one photon from $3snd$ states. Symmetry considerations and angular momentum selection rules constrain the angular distribution to be of the form

$$\frac{d\sigma}{d\Omega}(\theta)=\frac{I_0}{4\pi}[1+\beta P_2(\cos\theta)+\gamma P_4(\cos\theta)+\epsilon P_6(\cos\theta)]\ , \tag{1a}$$

where I_0 is the total integrated cross section, $P_k(\cos\theta)$ is the kth Legendre polynomial, and θ is the polar angle between the laser polarization and the direction of the emitted electron. The parameters I_0, β, γ, and ϵ are any real numbers. I_0 as a function of energy gives the total photoabsorption cross section, or line shape, of the transition. The three angular parameters β, γ, and ϵ vary as a function of energy; together they constitute the three parameter "spectra," which we measure and calculate in this paper.

To ensure that we were obtaining the expected angular distribution, we fixed the energy of all lasers and rotated the laser polarization under the electron detector 360° in increments of 10°. Since the ion signal does not depend on θ, we used any changes in it to correct the electron signal for changes in laser intensity and alignment during the measurement. To correct the electron signal, we simply divided it by the ion signal. Figure 3 shows the graph

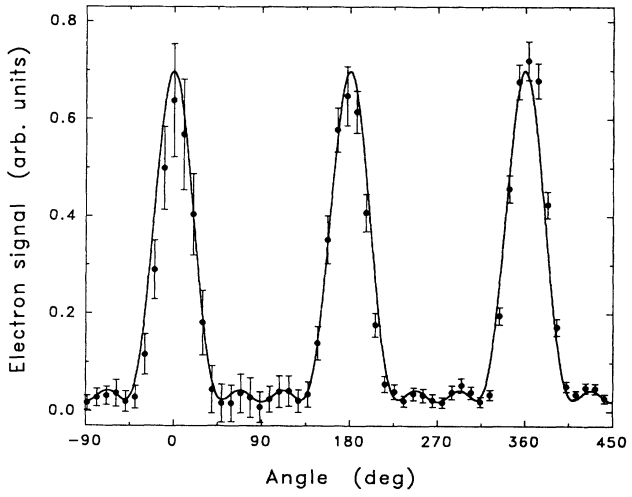

FIG. 3. Angular distribution of the corrected electron signal for the $3s10d\rightarrow 3p10d$ transition, with the third laser set to 35 660 cm^{-1}. This is the graph of the corrected signal from the electron detector as the laser polarization was rotated under it. All laser frequencies were fixed for these data. The solid line shows a fit of the theoretically predicted form of $d\sigma/d\Omega$ [Eq. (1a)] to the data points. The data agree quite well with the expected angular distribution. The fit gives results for the angular distribution parameters β, γ, and ϵ, as shown under method B in Table I.

of the corrected electron signal versus θ for the $3p\,10d$ state with the doubled third laser set at 35 660 cm^{-1}. The error bars show the 1σ error of the quotient, Gaussian propagated from the electron and ion signal Poisson errors. The solid line in Fig. 3 is the fit of Eq. (1) to these data points. The fit is quite good, and clearly the angular distribution is as expected. This fit gives precise numerical values for β, γ, and ϵ; these will be discussed later in this section. All of Fig. 3 corresponds to only one energy point in the spectra of β, γ, and ϵ. In principle, the procedure used to produce Fig. 3 could be repeated thousands of times with a slightly different third laser energy each time to produce parameter spectra as a function of photon energy.

We chose instead to use one electron detector at a particular angle, tuned the laser over the energy range, then changed the detector to another angle and tuned the laser again over the same range. For one particular $3pnd$ state, we typically took electron spectra at ten different angles θ, ranging from $\theta=0°$ to $\theta=90°$. Since the expected angular distribution is even about $\theta=0$ and periodic with period 180°, measuring on the interval [0°,90°] was all that was needed. At each energy point, we fit Eq. (1a) to the ten different electron signal values corresponding to each of the ten angles. At each energy point this produced fitted values for β, γ, and ϵ, thus providing angular distribution parameter spectra over the same energy range.

The problem with this procedure was that over the approximately five hours it took to collect ten electron spectra, the signal strengths would change due to unavoidable shifts in the lasers' power and alignment. These changes would mean that a comparison of electron signals taken at the beginning and end of the data-taking run would be meaningless, and a fit to them would give wrong results.

The ion signal, which does not depend on θ, was used to correct for these electron signal shifts. In principle, each ion signal, taken simultaneously with each electron signal, should be the same, regardless of θ. In practice, the ion signals varied according to the laser power and alignment. We divided each electron signal value at each energy point by the ion signal value taken simultaneously. Any fluctuation in the laser power or alignment would affect the electron and ion signal values in the same way. Taking the quotient cancels the fluctuations. This method of dividing the electron signal by its simultaneous ion signal also has the advantage of eliminating any effect due to varying optical saturation of the transition. Optical saturation, whether strong or weak at a particular energy, affects the electron and ion signal by the same factor, and so the effect cancels in the quotient.

The quotient can be written as

$$\frac{d\sigma}{d\Omega}\Big/\frac{I_0}{4\pi}=a_0+a_2P_2(\cos\theta)+a_4P_4(\cos\theta)+a_6P_6(\cos\theta)\ , \tag{1b}$$

since the ion signal is proportional to the total cross section I_0. Both sides of Eq. (1b) still contain an *a priori* unknown overall experimental normalization factor, due to the arbitrary experimental units of $d\sigma/d\Omega$ and I_0. Thus in general the fitted value of a_0 is not 1.0. The fitted value of a_0 determines the overall normalization. This normalization can be removed by taking the quotients $\beta=a_2/a_0$, $\gamma=a_4/a_0$, and $\epsilon=a_6/a_0$ since the same normalization factor is contained in a_0, a_2, a_4, and a_6.

The above procedure for normalizing the electron signals assumes that the relative efficiency of the electron and ion detector systems remained constant over the approximately five hours of a data-taking run. We thoroughly warmed up the apparatus and left the gate positions and widths, MCP voltages, and amplifier gains unchanged. The one uncontrollable efficiency factor was the intrinsic gain of the MCP's themselves, which did change over the space of some weeks. To confirm that this did not vary significantly during a data-taking run, we measured the $\theta=0$ electron signal at the beginning and end of each data-taking run, and several times in between the scans at other θ's. We saw that the ratio of the electron signal at $\theta=0$ to the ion signal did not change over the entire data-taking run.

For the fitting algorithm to work properly, the zero offset of the dc output of the gated integrators had to be adjusted so that the output was zero when a true zero signal occurred. Otherwise, in the case of a small signal plus a large zero offset, the fitting algorithm would interpret it as a large signal, and give erroneous results. For each scan, we carefully adjusted the zero offset to be less than 0.005 V out of a 5-V full scale signal. When the true signals fell to about 0.05 V, this uncertainty in the zero offset rendered our results meaningless. This effect limited us to scanning within about ± 200 cm^{-1} of the signal peak; in this energy range the signals were always at least 0.05 V.

For fitting purposes we used Eq. (1b), which is linear in the four fitted parameters a_0, a_2, a_4, a_6. We used the singular value decomposition method, as described in Ref. [25], to fit Eq. (1b) to the ten quotients of electron signal to simultaneous ion signal. The ten data points were taken at the ten different values of θ corresponding to one energy value. A separate fit was performed for each doubled third laser photon energy value in the range, producing fitted spectra of the a_0, a_2, a_4, and a_6 parameters. As expected, we found that the fitted values for a_0 were nearly constant as a function of energy. The actual fitted angular distribution parameters β, γ, and ϵ were obtained from $\beta=a_2/a_0$, $\gamma=a_4/a_0$, and $\epsilon=a_6/a_0$.

To show that the above procedure (method A) for fitting the ten electron signal spectra at the ten different angles θ to produce parameter spectra is valid, we measured the electron signal as a function of θ by manually rotating the laser polarizers, with the energies of all of the lasers fixed (method B). We then fit the resulting angular distribution to Eq. (1), as shown in Fig. 3. This fit gave values for the parameters β, γ, and ϵ, shown in the row for method B in Table I. Selecting the values of β, γ, and ϵ at that same single energy point from the $3p\,10d$ parameter spectra gives the values for β, γ, and ϵ shown in the row for method A in Table I. Method B is the more traditional way to obtain angular distributions, but as our errors in the method A parameter values are about 0.5 (as we shall discuss later), the two methods are equally valid.

TABLE I. Comparison of measured values of angular distribution parameters of the $3p10d$ state at 35 660 cm^{-1}. Method A is used for the parameter spectra shown in this paper. It involves scanning the third laser energy to get electron signal spectra at ten different angles θ, then fitting those ten data points to Eq. (1) to obtain the β, γ, and ϵ. The row for method A shows just one energy point out of many from the $3p10d$ parameter spectra obtained in this manner. Method B involves fixing the energies of all of the lasers, then manually rotating the polarization of all of them to vary θ. We obtain the graph shown in Fig. 3, then fit it to Eq. (1) and obtain β, γ, and ϵ at a single energy. The good agreement between the two methods shows that both are equally valid. For comparison the theory values derived in Sec. III for the parameters of this state at this energy are also shown.

	β	γ	ϵ
Method A	2.5(5)	2.6(5)	1.2(5)
Method B	2.6(2)	2.7(2)	1.5(2)
Theory	2.51	2.81	2.00

Only method A allows the convenient generation of angular distribution parameter spectra as a function of energy.

For the rest of this paper we use signals obtained with θ in the range [0°,90°]. As seen in Fig. 3 the measured angular distribution is not perfectly periodic with period 180°. This means that the angular distribution and parameters obtained with θ in the range, e.g., [90°,180°], will not be exactly the same. However, the fitted parameters derived from two different angle ranges differ by no more than 0.3, well within our ultimate error bar of 0.5.

Only four nonzero Legendre polynomial coefficients are allowed in Eq. (1b), as will be shown in Sec. III. However, due to noise and error in the experimental data, our measured $d\sigma(\theta)/d\Omega$ may have nonzero values for a_1, a_3, a_5, a_7, a_8, etc. We found that when we fit our data to $\sum_n a_n P_n(\cos\theta)$, where $n=0,2,4,6,7,8$ and $n=0,2,4,6,8,10$, we obtained essentially the same values for a_0,a_2,a_4,a_6 as fitting the data to Eq. (1b). At the same time the values for a_7,a_8, or a_8, a_{10}, were consistent with zero. Including a_1, a_3, or a_5 in the fit caused a total loss of significance for all of the a_n values. Thus coefficients of order 7 or more were zero when included in the fit, and coefficients of order 1, 3, 5 are not defined when they are fit to our data, as expected.

III. THEORY

In order to derive specific formulas for the β, γ, and ϵ parameters in Eq. (1a), we must start from the most general formula for $d\sigma/d\Omega$ of an atom absorbing a linearly polarized photon and then emitting an electron:

$$\frac{d\sigma}{d\Omega}=N^2\sum_{J_c,J_{cs},M_{cs}}\left|\sum_{l,m,J,M_J}Y_{lm}(\hat{\mathbf{k}})\langle J_{cs}M_{cs}lm\,|JM_J\rangle\langle(J_{cs}l)JM_J-|\hat{\boldsymbol{\epsilon}}\cdot\mathbf{r}|J_0 0\rangle\right|^2 . \tag{2}$$

This equation introduces most of the notation used in the rest of this paper. N^2 is a normalization constant. $\mathbf{J}_c$ is the total residual ion core angular momentum. $\mathbf{J}_{cs}=\mathbf{J}_c+\mathbf{s}$, where $\mathbf{s}$ is the spin of the outer photoelectron; M_{cs} is the projection of $\mathbf{J}_{cs}$ on the axis defined by the laser polarization. l and m are the orbital angular momentum of the outer electron and its projection. $\mathbf{J}$ and M_J are the total angular momentum of the system, and its projection on the axis of quantization; $\mathbf{J}=\mathbf{J}_{cs}+\mathbf{l}$. $\hat{\mathbf{k}}$ is the vector in the direction of the ejected electron's travel. The minus sign in the second matrix element indicates that the wave functions are normalized according to incoming-wave boundary conditions. $\hat{\boldsymbol{\epsilon}}$ is the unit polarization vector of the last laser photon. The light is linearly polarized. $\mathbf{r}$ is the position of the Rydberg electron relative to the ion core. J_0 and 0 are the initial total angular momentum of the Rydberg Mg atom before absorption of the third laser photon, and its projection on the axis of quantization. Due to the parallel linear polarization of our lasers, the $3snd$ states we use have $J_0=2$, and the $3pnd$ states have $J=1$ or 3.

Equation (2) can be expanded as

$$\frac{d\sigma}{d\Omega}=N^2\sum_{\substack{J_c,J_{cs}\\ l,l',J,J'}}\sum_{\substack{m,m',M_{cs}\\ M_J,M_{J'}}}Y^*_{l'm'}(\hat{\mathbf{k}})Y_{lm}(\hat{\mathbf{k}})\langle J'M_{J'}|J_{cs}M_{cs}l'm'\rangle\langle J_{cs}M_{cs}lm\,|JM_J\rangle\langle J_0 0|\hat{\boldsymbol{\epsilon}}^*\cdot\mathbf{r}|[(J_c s)J_{cs}l]JM_J-\rangle$$
$$\times\langle[(J_c s)J_{cs}l']J'M_{J'}-|\hat{\boldsymbol{\epsilon}}\cdot\mathbf{r}|J_0 0\rangle . \tag{3}$$

Equation (3) can be written with reduced matrix elements as

$$\frac{d\sigma}{d\Omega}=N^2\sum_{\substack{J_c,J_{cs}\\ l,l',J,J'}}\left[\sum_{m,M_{cs}}Y^*_{l'm}(\hat{\mathbf{k}})Y_{lm}(\hat{\mathbf{k}})\langle J'0|J_{cs}M_{cs}l'm\rangle\langle J_{cs}M_{cs}lm\,|J0\rangle\frac{\langle J_0 0|10J0\rangle}{[J_0]}\frac{\langle J'0|10J_0 0\rangle}{[J']}\right]$$
$$\times\langle J_0\|r^{(1)}\|[(J_c s)J_{cs}l]J-\rangle\langle[(J_c s)J_{cs}l']J'-\|r^{(1)}\|J_0\rangle , \tag{4}$$

where $r^{(1)}$ is a first-rank tensor, and $[x]$ is defined as $(2x+1)^{1/2}$. The portion of Eq. (4) in the large brackets, called A, can be written as

$$A=\begin{bmatrix}J_0 & 1 & J\\ 0 & 0 & 0\end{bmatrix}\begin{bmatrix}J' & 1 & J_0\\ 0 & 0 & 0\end{bmatrix}\sum_{m,M_{cs}}(-1)^m\sum_k\frac{[l][l']}{[k](4\pi)^{1/2}}\langle l'0l0|k0\rangle$$

$$\times Y_{k0}(\hat{\mathbf{k}})\langle k0|l'-mlm\rangle\langle J'0|J_{cs}M_{cs}l'm\rangle\langle J_{cs}M_{cs}lm|J0\rangle\ , \tag{5}$$

using the formulas for the product of Y_{lm} functions [26]. The Y_{k0} function can be written in terms of $P_k(\cos\theta)$, giving

$$A=\frac{-1}{4\pi}[J][J'][l][l']\begin{bmatrix}J_0 & 1 & J\\ 0 & 0 & 0\end{bmatrix}\begin{bmatrix}J' & 1 & J_0\\ 0 & 0 & 0\end{bmatrix}\sum_k[k]^2P_k(\cos\theta)\begin{bmatrix}l' & l & k\\ 0 & 0 & 0\end{bmatrix}$$

$$\times\left[\sum_{m,m',M_{cs}}(-1)^m\begin{bmatrix}l' & l & k\\ m' & -m & 0\end{bmatrix}\begin{bmatrix}J_{cs} & l' & J'\\ M_{cs} & m' & 0\end{bmatrix}\begin{bmatrix}J_{cs} & l & J\\ M_{cs} & m & 0\end{bmatrix}\right]. \tag{6}$$

The portion of Eq. (6) in large brackets, called B, is

$$B=(-1)^{J_{cs}}\begin{bmatrix}k & J' & J\\ 0 & 0 & 0\end{bmatrix}\begin{Bmatrix}k & J' & J\\ J_{cs} & l & l'\end{Bmatrix}. \tag{7}$$

By using the identity 6.2.8 of Ref. [27] the m dependences of the angular distribution are removed.

Combining Eqs. (3)–(7) we obtain

$$\frac{d\sigma}{d\Omega}=\sum_k a_kP_k(\cos\theta)\ , \tag{8a}$$

where

$$a_k=\frac{-N^2}{4\pi}\sum_{\substack{J_c,J_{cs}\\ l,l',J,J'}}(-1)^{J_{cs}}[J][J'][l][l'][k]^2\begin{bmatrix}J_0 & 1 & J\\ 0 & 0 & 0\end{bmatrix}\begin{bmatrix}J' & 1 & J_0\\ 0 & 0 & 0\end{bmatrix}\begin{bmatrix}l' & l & k\\ 0 & 0 & 0\end{bmatrix}\begin{bmatrix}k & J' & J\\ 0 & 0 & 0\end{bmatrix}$$

$$\times\begin{Bmatrix}k & J' & J\\ J_{cs} & l & l'\end{Bmatrix}\langle J_0\|r^{(1)}\|[(J_cs)J_{cs}l]J-\rangle\langle[(J_cs)J_{cs}l']J'-\|r^{(1)}\|J_0\rangle\ . \tag{8b}$$

For the rest of this paper the reduced matrix elements in Eq. (8b) are abbreviated as $D^*_{J_{cs}J}$ and $D_{J_{cs}J'}$, respectively. Only four terms in the summation of Eq. (8a) are nonzero due to the triangle rule for the $3j$ symbols. The nonzero terms have $k=0,2,4,6$, confirming the form of Eqs. (1a) and (1b). Thus Eq. (8a) matches Eq. (1a), with $I_0=4\pi a_0$, $\beta=a_2/a_0$, $\gamma=a_4/a_0$, and $\epsilon=a_6/a_0$. Note that in calculating β, γ, and ϵ, the normalization N^2 cancels out. For our particular final states, we can have $J_{cs}=0$ or 1, since $J_c=\frac{1}{2}$, $s=\frac{1}{2}$, $l=J$, and $l'=J'$. When $l=J=1$ the ejected electron is an outgoing p wave. When $l=J=3$ the electron is an outgoing f wave. There are in general eight terms in the summation of Eq. (8b). Some of these terms are zero, depending on k.

Evaluating Eq. (8a) with the aid of $3j$ and $6j$ tables, we calculate the angular distribution parameters in terms of the reduced matrix elements

$$a_0=\tfrac{2}{15}(|D_{01}|^2+|D_{11}|^2)+\tfrac{3}{35}(|D_{03}|^2+|D_{13}|^2)\ , \tag{9a}$$

$$a_2=\tfrac{2}{15}(2|D_{01}|^2-|D_{11}|^2)+\tfrac{1}{35}(4|D_{03}|^2+3|D_{13}|^2)$$
$$-\tfrac{6}{35}[\sqrt{6}\,\mathrm{Re}(D^*_{01}D_{03})+2\,\mathrm{Re}(D^*_{11}D_{13})]\ , \tag{9b}$$

$$a_4=\tfrac{9}{385}(6|D_{03}|^2+|D_{13}|^2)$$
$$-\tfrac{2}{35}[4\sqrt{6}\,\mathrm{Re}(D^*_{01}D_{03})-6\,\mathrm{Re}(D^*_{11}D_{13})]\ , \tag{9c}$$

$$a_6=\tfrac{5}{77}(4|D_{03}|^2-3|D_{13}|^2)\ , \tag{9d}$$

$$\beta=a_2/a_0,\quad \gamma=a_4/a_0,\quad \epsilon=a_6/a_0\ . \tag{9e}$$

$D_{J_{cs}J}$ is written out in Eq. (8b). Up to this point, our derivation is completely general, and we have not used MQDT.

Next we calculate the reduced matrix elements. This is where MQDT is essential. We have two manifolds of states, $J=1$ and $J=3$. For each manifold the derivations proceed in parallel; they are brought together only in Eq. (9). We use seven $J=1$ channels and eight $J=3$ channels. They can be described in J_cJ_{cs} or LS coupling. In

LS coupling the states are $3s\epsilon p\ ^1P_1$, $3pns\ ^1P_1$, $3pnd\ ^1P_1$, $3s\epsilon p\ ^3P_1$, $3pns\ ^3P_1$, $3pnd\ ^3P_1$, $3pnd\ ^3D_1$, and $3pnd\ ^3D_3$, $3s\epsilon f\ ^1F_3$, $3pnd\ ^1F_3$, $3png\ ^1F_3$, $3s\epsilon f\ ^3F_3$, $3pnd\ ^3F_3$, $3png\ ^3F_3$, $3png\ ^3G_3$. In J_cJ_{cs} coupling the states ϕ_i^J are, for $J=1$, $3s_{1/2}\{0\}\epsilon p$, $3s_{1/2}\{1\}\epsilon p$, $3p_{1/2}\{1\}ns$, $3p_{3/2}\{1\}ns$, $3p_{1/2}\{1\}nd$, $3p_{3/2}\{1\}nd$, and $3p_{3/2}\{2\}nd$. For $J=3$ the states are $3s_{1/2}\{0\}\epsilon f$, $3s_{1/2}\{1\}\epsilon f$, $3p_{1/2}\{1\}nd$, $3p_{3/2}\{1\}nd$, $3p_{3/2}\{2\}nd$, $3p_{1/2}\{1\}ng$, $3p_{3/2}\{1\}ng$, and $3p_{3/2}\{2\}ng$. The number in braces is J_{cs}. Near the nucleus, LS coupling is the most physical due to the large electrostatic and exchange forces. At large distances the rate of phase accumulation depends on the energy of the core state, which in turn depends on L_c, S_c, and J_c. L_c and S_c are the total orbital angular momentum and spin of the core; $\mathbf{J}_c=\mathbf{L}_c+\mathbf{S}_c$. At large distances J_cJ_{cs} coupling is appropriate (actually jj and jK coupling [28] are as applicable as J_cJ_{cs}, but the matrix elements needed to describe the current angular distribution experiment are easier to evaluate in J_cJ_{cs} coupling). The $\underline{K}$ (reaction-reactance) matrix in J_cJ_{cs} coupling can be obtained from the $\underline{K}$ matrix in LS coupling through a simple transformation that represents the recoupling of the angular momenta and spins

$$K^J_{J_cJ_{cs}}=V^J_{J_cJ_{cs}-LS}K^J_{LS}V^{\dagger J}_{LS-J_cJ_{cs}}\ , \tag{10}$$

where

$$\begin{aligned}V^J_{J_cJ_{cs}-LS}&=\langle\{[(L_cS_c)J_cs]J_{cs}l\}J|[(L_cl)L(S_cs)S]J\rangle\\&=\langle[(L_cS_c)J_cs]J_{cs}|[L_c(S_cs)S]J_{cs}\rangle\langle[(L_cS)J_{cs}l]J|[(L_cl)LS]J\rangle\\&=(-1)^{2J_{cs}+L_c+S_c+s+S+l+L}[J_c][S][J_{cs}][L]\begin{Bmatrix}L_c&S_c&J_c\\s&J_{cs}&S\end{Bmatrix}\begin{Bmatrix}S&L_c&J_{cs}\\l&J&L\end{Bmatrix}.\end{aligned} \tag{11}$$

The treatment derived here is similar in spirit to the more usual LS to jj recoupling [4], but is more appropriate for the current experiment. The values of $\underline{K}^{J=1}_{LS}$ and $\underline{K}^{J=3}_{LS}$ are given in Tables II and III. These were calculated using a box of radius 20 a.u., larger than the 12 a.u. box used for calculation of previous $\underline{K}$ matrices [2,3]. The new $\underline{K}^{J=3}_{LS}$ matrix also includes the $3png\ ^1F_3$, $3png\ ^3F_3$, and $3png\ ^3G_3$ channels. In all that follows, the K^J_{ij} values used are from the J_cJ_{cs} coupled $\underline{K}$ matrix. The larger R-matrix box for $r_0=20$ a.u. should in principle incorporate some longer-range multipole effects that were neglected beyond 12 a.u. in the previous $\underline{K}$ matrices [2,3]. These multipole effects appear to be negligible, based on the good agreement between calculations conducted using the different $\underline{K}$ matrices. The inclusion of $3png$ channels in the newer $\underline{K}$ matrices allows us to describe additional weak and narrow g-wave resonances. Overall these have only minor importance, but a few experimental and theoretical features derive from g-wave resonances, as we shall discuss later.

In a standard formulation of MQDT the jth independent wave function (prior to imposing boundary conditions at $r\rightarrow\infty$) can be written as

$$\psi^J_j=\mathcal{A}\sum_i\phi^J_i(f_i\delta_{ij}-g_iK^J_{ij})\ , \tag{12}$$

when the outer electron is at distances larger than r_0. All wave functions ψ are functions of the energy. i and j run over the states (channels) listed above. $f_i(g_i)$ is the regular (irregular) Coulomb function of energy $\varepsilon_i=E-E_i$ and angular momentum l_i. E_i is the ionic core energy associated with the core of the ith channel, shown in Table

TABLE II. $\underline{K}^{J=1}$ matrix. The 7×7 matrix is evaluated at three different energies (relative to the Mg ground state). All matrix elements not included in the three block-diagonal submatrices shown here are zero.

	LS coupled states						
Energy	^1P			^3P			^3D
(cm^{-1})	$3s\epsilon p$	$3pns$	$3pnd$	$3s\epsilon p$	$3pns$	$3pnd$	$3pnd$
95 149	−1.29	2.71	0.860	0.158	0.235	0.112	
	2.71	−5.38	−1.77	0.235	−2.20	−0.0758	
	0.860	−1.77	−0.823	0.112	−0.0758	0.590	0.616
97 344	−1.36	2.89	0.900	0.145	0.248	0.0999	
	2.89	−5.87	−1.90	0.248	−2.28	−0.0823	
	0.900	−1.90	−0.824	0.0999	−0.0823	0.600	0.637
99 538	−1.38	3.00	0.910	0.133	0.264	0.0894	
	3.00	−6.25	−1.98	0.264	−2.35	−0.0924	
	0.910	−1.98	−0.807	0.0894	−0.0924	0.607	0.666

TABLE III. $\underline{K}^{J=3}$ matrix. The 8×8 matrix is evaluated at three different energies (relative to the Mg ground state). All matrix elements not included in the four block-diagonal submatrices shown here are zero.

	LS coupled states							
Energy	^3D	^1F			^3F			^3G
(cm^{-1})	3*pnd*	3*sεf*	3*pnd*	3*png*	3*sεf*	3*pnd*	3*png*	3*png*
95 149		0.317	0.524	−0.0452	0.333	0.731	−0.0557	
	0.616	0.524	−0.269	0.0116	0.731	2.00	−0.100	
		−0.0452	0.0116	−0.0608	−0.0557	−0.100	−0.0552	0.0881
97 344		0.306	0.552	−0.0400	0.310	0.674	−0.0473	
	0.637	0.552	−0.256	0.0203	0.674	1.86	−0.101	
		−0.0400	0.0203	−0.0643	−0.0473	−0.101	−0.0574	0.0992
99 538		0.295	0.577	−0.0422	0.293	0.629	−0.0461	
	0.666	0.577	−0.236	0.0260	0.629	1.76	−0.110	
		−0.0422	0.0260	−0.0640	−0.0461	−0.110	−0.0548	0.105

IV. E is the total energy of the excited state (above the Mg ground state). K_{ij}^J is the $\underline{K}$ matrix in J_cJ_{cs} coupling. $\mathcal{A}$ is the antisymmetrization operator (which has no effect since the electrons are in different regions of space). $\phi_i^J=\chi_i|\{[(L_c^iS_c)J_c^is]J_{cs}^il_i\}J\rangle$ are the J_cJ_{cs} states. χ_i is the radial core function associated with the ionic core state. All of the ψ_i^J states we consider have one of three possible core states: $3s_{1/2}$, $3p_{1/2}$, or $3p_{3/2}$.

The wave function of the 3*snd* "initial state" being photoionized can be written in a similar manner when the outer electron is at distances larger than r_0:

$$|J_0\rangle=\psi_0^{J_0}=\mathcal{A}\phi_0^{J_0}(\cos\pi\mu_0 f_0-\sin\pi\mu_0 g_0)/\nu_0^{3/2}\ , \quad (13)$$

where $\chi_0=\chi_{3s}$, $L_c^0=0$, $S_c^0=\frac{1}{2}$, $J_c^0=\frac{1}{2}$, $J_{cs}^0=0$, $l_0=2$, $J_0=2$, and μ_0 is the quantum defect of the initial state. ν_0 is the effective quantum number of the 3*snd* state given by $\nu_0=[R/(E_{3s}-E)]^{1/2}$. R is the Rydberg constant for Mg: 109 734.86 cm^{-1}. We have taken advantage of the fact that the initial-state LS coupling, 3*snd* ^1D is identical to the J_cJ_{cs} coupling given here. In the isolated-core approximation the dipole operator only acts on the core electron due to the fact that the outer electron spends so little time near the nucleus that it cannot absorb a photon. Using this approximation the reduced dipole operator connecting MQDT wave functions (12) and (13) is

$$\begin{aligned} d_j^J&=\langle\psi_j^J\|r^{(1)}\|\psi_0^{J_0}\rangle \\ &\cong\sum_i\langle\phi_i^J\|r^{(1)}\|\phi_0^{J_0}\rangle \\ &\quad\times\int_{r_0}^{\infty}(\cos\pi\mu_0 f_0-\sin\pi\mu_0 g_0) \\ &\quad\times(f_i\delta_{ij}-g_iK_{ij}^J)dr/\nu_0^{3/2}\ . \end{aligned} \quad (14)$$

Here again i and j run over the possible channels listed at the beginning of this section.

We derive an expression for $\langle\phi_i^J\|r^{(1)}\|\phi_0^{J_0}\rangle$ based on the repeated application of the formula for a tensor operator that only acts on a part of a coupled system (Eq. 7.1.7 of Ref. [27]). Due to the appearance of a zero in each of the resulting 6*j* coefficients, this expression reduces to a very simple formula

$$\begin{aligned}\langle\phi_i^J\|r^{(1)}\|\phi_0^{J_0}\rangle&=\delta_{l_il_0}\delta_{J_{cs}^i1}\delta_{L_c^i1}[J][J_c^i](-1)^{3/2-J_c^i+J_0+l_0} \\ &\quad\times\int_0^{\infty}\chi_i r\chi_0 dr/3\sqrt{2}\ . \end{aligned} \quad (15)$$

In deriving Eq. (15) we used the fact that $L_c^0=0$, $J_{cs}^0=0$. Equation (15) applies to all isolated core experiments where the initial state is $msnl_0\,^1L$. We do not need to know the value of the dipole matrix element between χ_0 and χ_i to obtain relative cross sections and angular distributions, since it is common to all of the nonzero terms.

Finally we obtain a value for the overlap of the outer electron's Coulomb functions by using Green's theorem:

$$\begin{aligned}\int_{r_0}^{\infty}(\cos\pi\mu_0 f_0-\sin\pi\mu_0 g_0)(f_i\delta_{ij}-g_iK_{ij}^J)dr/\nu_0^{3/2}&=\nu_0^2\nu_i^2W(f_0\cos\pi\mu_0-g_0\sin\pi\mu_0,f_i\delta_{ij}-g_iK_{ij}^J)/[\nu_0^{3/2}(\nu_i^2-\nu_0^2)] \\ &\cong 2\nu_i^2\sqrt{\nu_0}(\sin\pi\mu_0\delta_{ij}-\cos\pi\mu_0K_{ij}^J)/[\pi(\nu_i^2-\nu_0^2)]\ , \end{aligned} \quad (16)$$

where $W(F,G)=FG'-F'G$ is the radial Wronskian evaluated at $r=r_0$, and $\nu_i=[R/(E_i-E)]^{1/2}$ is the effective quantum number in channel i. The last approximate step in Eq. (16) results from ignoring the energy dependence of the f and g at the small radius r_0, while using $W(f,g)=2/\pi$ and $W(f,f)=W(g,g)=0$. Equation (16) contains the usual isolated-core approximations but is cast in a form more amenable to MQDT manipulations. We now combine the two pieces (15) and (16) into the full dipole matrix element to obtain

TABLE IV. Core energies of the Mg atom. Each energy given amounts to the energy necessary to remove one electron from the neutral atom and leave the Mg^+ core in the given state. E_{3s} is simply the ionization energy of Mg. Energies are in cm^{-1} above the ground state, with the neutral atom ground state defined to have zero energy.

E_{3s}	61 671.02
$E_{3p1/2}$	97 340.33
$E_{3p3/2}$	97 431.90

$$d_j^J = C(-1)^{J_0}[J] \times \sum_i \delta_{l_i l_0}\delta_{J_{cs}^i 1}\delta_{L_c^i 1}[J_c^i](-1)^{3/2-J_c^i+l_0} \times \nu_i^2(\sin\pi\mu_0\delta_{ij} - \cos\pi\mu_0 K_{ij}^J)/(\nu_i^2-\nu_0^2) , \quad (17)$$

where C is a factor common to all of the d_j^J:

$$C = \sqrt{2\nu_0}\int_0^\infty \chi_{3p} r \chi_{3s} dr/3\pi . \quad (18)$$

We approximate C to be the same whether it includes $\chi_{3p_{1/2}}$ or $\chi_{3p_{3/2}}$.

We construct the physical wave functions and dipole matrix elements by superposing the independent wave functions in Eq. (12) to eliminate exponentially diverging terms in the closed channels and satisfy normalization per unit energy in the open channels. The equations these coefficients must satisfy are the following. When j is a closed channel, $\varepsilon_j = E - E_j < 0$, and

$$\sum_i (\tan\beta_j\delta_{ji} + K_{ji}^J) A_{i\rho}^J = 0 , \quad (19a)$$

where $\beta_j = \pi(\nu_j - l_j)$. When j is an open channel (i.e., $\varepsilon_j > 0$),

$$\sum_i \delta_{ji} A_{i\rho}^J = T_{j\rho}^J \cos\pi\tau_\rho^J \quad (19b)$$

and

$$\sum_i K_{ji}^J A_{i\rho}^J = T_{j\rho}^J \sin\pi\tau_\rho^J . \quad (19c)$$

The $\underline{T}^J$ matrix in Eqs. (19) is unitary. Since we have two open channels, ρ runs from 1 to 2. Equations (19) can be combined in the usual way to obtain a generalized eigensystem where $\tan\pi\tau_\rho^J$ are the eigenvalues and $A_{i\rho}^J$ are the eigenvectors. The physical dipole matrix elements are obtained by superposition,

$$d_\rho^J = \sum_j d_j^J A_{j\rho}^J , \quad (20a)$$

or in a more conventional form, assuming only closed channels contribute,

$$d_\rho^J = C(-1)^{J_0}[J]\sum_i \delta_{l_i l_0}\delta_{J_{cs}^i 1}\delta_{L_c^i 1}[J_c^i](-1)^{3/2-J_c^i+l_0} \times \frac{\nu_i^2\sin\pi(\nu_i-\nu_0)}{(\nu_i^2-\nu_0^2)\cos\pi\nu_i} A_{i\rho}^J . \quad (20b)$$

The d_ρ^J are real reduced dipole matrix elements that govern the transition from the ground state to the real wave function ψ_ρ^J. This standing wave does not satisfy boundary conditions corresponding to the experiment (with an electron escaping in a specific direction). This necessitates one further transformation to the solutions obeying the "incoming-wave boundary conditions," with outgoing waves only in channel i. The incoming-wave boundary condition is needed to represent a solution corresponding to photoelectron flux that escapes as a plane wave toward the detector only in channel i at times $t \to \infty$. A clear discussion is given by Starace [29]. The final wave function is

$$\psi_j^{J-} = \sum_\rho \psi_\rho^J T_{j\rho}^J \exp[i(l_j\pi/2 - \pi\tau_\rho^J - \sigma_j)] , \quad (21)$$

where σ_j is the Coulomb phase shift in channel j, $\sigma_j = \arg\Gamma[l_j+1-i/(2\varepsilon_j)^{1/2}]$, and ε_j is in atomic units. This final transformation achieves the goal of constructing a wave function that matches the experiment. We can now obtain the matrix elements needed for Eqs. (8b):

$$D_{J_{cs}^j J} = \sum_\rho d_\rho^J T_{j\rho}^J \exp[i(-l_j\pi/2 + \pi\tau_\rho^J + \sigma_j)] . \quad (22)$$

The values of the $T_{j\rho}$ and $A_{j\rho}^J$ contained in d_ρ^J are obtained by solving Eqs. (19). Equations (8) can now be used to generate cross sections and angular distributions.

To summarize, the sequence of transformations beginning with Eq. (10) is able to convert the dynamical information contained in nonrelativistic reaction matrices into photoionization cross sections and angular distributions obtained in isolated-core experiments. The necessary $\underline{K}$ matrices are obtained from nonrelativistic R-matrix calculations. Since all of the other dynamical information is exact, the comparison of the current theory with experiment, described in Sec. IV, directly reflects on the precision of the R-matrix calculations.

IV. RESULTS AND DISCUSSION

A. Results

For each $3snd \to 3pnd$ transition, we have measured the ion signal yielding the total photoionization cross section. These line shapes have been measured and compared with theory in Ref. [3]. Our measured line shapes agree with those in Ref. [3], and they agree quite well with theory, as shown in Ref. [3].

Our measurements of the angular distribution parameters β, γ, and ϵ are shown in Figs. 4, 5, and 6. The superimposed smooth solid lines are the MQDT predictions for the parameters. Figure 4 shows the parameters for the $3s\,10d \to 3p\,10d$ transition, over a range of 400 cm^{-1} centered on the peaks of the transition. Figure 5 shows the $3s\,12d \to 3p\,12d$ transition over the same energy range as Fig. 4. Figure 6 shows the $3s\,18d \to 3p\,18d$ transition over a narrower energy range to better exhibit the narrower features of the higher n spectra. In each graph, the parameters have the same vertical scale but are offset vertically for the sake of clarity. In each case the theoretical prediction was convolved with the 1 cm^{-1} instrumental linewidth of our measurements, reducing the sharpness of some of the narrow features, especially in

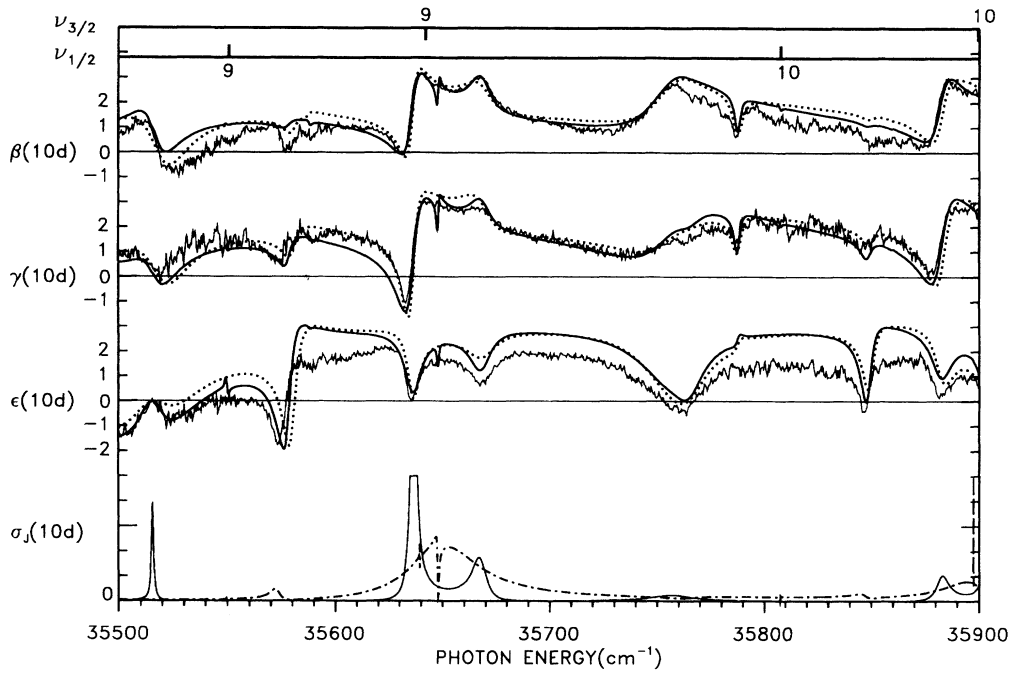

FIG. 4. Angular distribution parameters β, γ, and ϵ for the $3s\,10d \rightarrow 3p\,10d$ transition. The experimental results are shown with the jagged solid line. The error of our derived values for β, γ, and ϵ vary across the graph, however, a typical 1σ error for the parameters is 0.5. The predictions of the $\underline{K}$ matrix-MQDT theory as described in the main text are shown with a smooth solid line. The results of the alternate MQDT theory formulation using earlier $\underline{K}$ matrices of Refs. [2,3], described in the Appendix, are shown as a dotted line. Each horizontal line indicates the zero for the corresponding parameter that overlaps it. σ_J is the relative photoionization cross section (in arbitrary units) contributed by the $J=1$ (solid curve) and $J=3$ (dash-dotted curve) final states. The narrowest peak heights have been artificially chopped off. Unlike the parameters β, γ, and ϵ, the cross section has not been convoluted with the experimental resolution (1 cm^{-1}). The top of the figure shows the effective quantum number scales going to the two $3p_{1/2}$ and $3p_{3/2}$ fine-structure thresholds in unit steps.

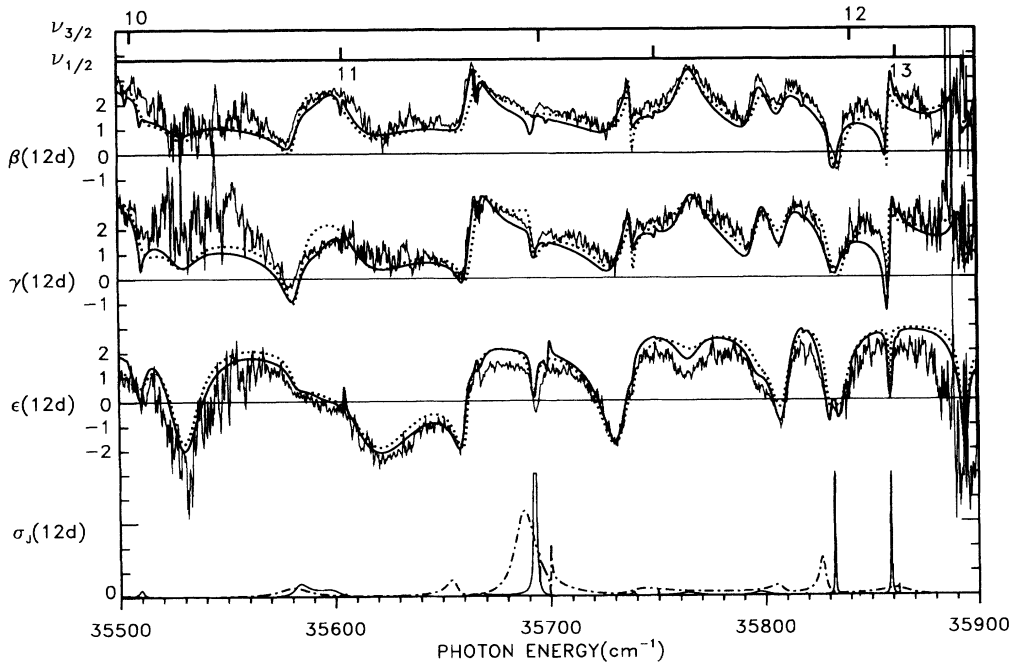

FIG. 5. Angular distribution parameters β, γ, and ϵ for the $3s\,12d \rightarrow 3p\,12d$ transition. The comments of Fig. 4 apply to this graph.

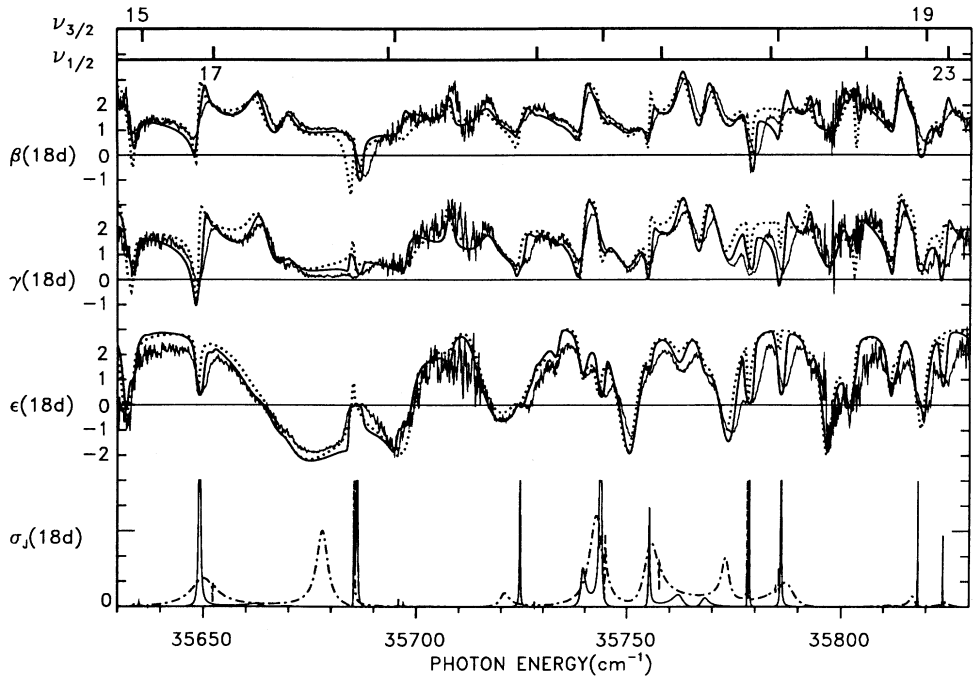

FIG. 6. Angular distribution parameters β, γ, and ϵ for the $3s18d \rightarrow 3p18d$ transition. The comments of Fig. 4 apply to this graph.

the $n=18$ parameters. The positions of the unperturbed Mg^+ ion transitions $3s_{1/2} \rightarrow 3p_{1/2}$ and $3p_{3/2}$ are at positions 35 669 cm^{-1} and 35 761 cm^{-1}, respectively. Although we measured the angular distribution parameters for all of the $3pnd$ states with $n=10-18$, we show only three sets of parameters. All differ in detail, but exhibit similar qualitative features and shapes. For $n \geq 19$, the features of the spectra became quite narrow, and our laser linewidth was a limiting factor.

The errors in our values for β, γ, and ϵ come from several sources, listed below in order from largest to smallest. The two largest sources of error are random in nature, and are due to the random fluctuations (noise) in the signal levels, when all of the lasers are fixed in frequency and the signal should remain constant. The largest error comes from the self-consistency, or repeatability, of our results for the angular distribution parameters. We checked this by going through the data analysis procedure of Sec. II using different sets of electron signals at certain angles, all corresponding to the same transition. That is, instead of using all of the measured electron signals at, e.g., $\theta=0°, 21°, 31°, 34°, 49°, 55°, 62°, 70°, 76°, 90°$, we used just four electron spectra at $\theta=0°, 31°, 55°, 90°$ and fit Eq. (1b) to them. (The angles were chosen to be extremes or roots of the various Legendre polynomials, and to be distributed as evenly as possible over the range 0–90°.) We did this for several different sets of four out of ten angles. The angular distribution parameter spectra obtained agreed with each other to within approximately 0.3 or less at the peaks of the line shapes. (The numbers for the angular distribution parameters have no units.)

The other random error due to noise in the signals appeared as the fitting error. In essence this error reveals the consistency of our data with Eq. (1b). The standard deviations of β, γ, and ϵ due to the fitting error were obtained via Gaussian error propagation from the fitting errors for the parameters a_0, a_2, a_4, a_6. The a_k fitting errors were the square roots of the diagonal elements of the covariance matrix returned by the fitting algorithm [25]. These fitting errors represent the minimum error possible. These errors depend on the estimate of error of our electron signal to ion signal quotients; the quotient error was obtained via Gaussian error propagation from the Poisson errors of the electron and ion signals. The quotient errors were in the range [0.01, 0.15]. The fitted values of β, γ, and ϵ were insensitive to these input error values. The fitting errors of β, γ, and ϵ were very small at energies corresponding to peaks of the line shapes, but grew to about 1.0 at energies where the electron and ion signal values were very small. This indicated that at small electron signal values, where $d\sigma/d\Omega$ and I_0 were nearly zero, the parameters β, γ, and ϵ were not well defined, due to the form of Eq. (1a).

The rest of the errors, smaller in magnitude than the two previously described, were systematic in nature. It is possible that the angle θ at which we set the laser polarization was in fact $\theta+\delta$. δ would have been the same for all θ. This systematic offset of θ could be caused, for example, by a tilt of the linear polarizers relative to the vacuum chamber and detectors. The fitting algorithm, using the misrepresented values of θ for the electron signals, would then return incorrect values for β, γ, and ϵ. We estimate δ for our apparatus is less than 2°. We simulated this effect of nonzero δ by generating on a computer electron signals at various θ from a given angular distribution described by β, γ, and ϵ. The angles θ were altered to be

$\theta+\delta$, and the electron signals labeled by their altered angles were then treated as real data and fit to Eq. (1), generating new β', γ', and ϵ'. For $|\delta| \leq 2°$ the original and transformed angular distribution parameters agreed to within approximately 0.2 or less. For $|\delta| \geq 5°$ the transformed parameters β', γ', and ϵ' were drastically changed from their original values, so accurate angular alignment was critical.

Another systematic error could be caused by a nonzero offset to the dc signal level outputs of the gated integrators. As described earlier, we carefully set the offset to be no more than a tenth of the signal for each scan. Artificially shifting the dc offset of some or all of the electron signals in a set by 1 part in 10 had no noticeable effect on the parameters. The ion signals in general were larger than the electron signals, and their zero offset was always a small fraction of their signal value over the energy ranges examined.

A final possible systematic error is due to the nonzero solid angle of our detector. The finite size of the detector caused it to convolve or average the angular distribution over its 0.2 radian width. We simulated this effect by calculating the angular distribution at each energy from theoretically generated parameter spectra and averaging it over a 0.2 radian width. Then we treated that averaged angular distribution as real data and fit Eq. (1) to it. Repeating this procedure at each energy generated new parameter spectra. At a detector width of 0.2 radians, the β and γ spectra did not change at all. The ϵ parameter, since it multiplies $P_6(\cos\theta)$, which varies the most rapidly with θ, would be expected to be the most sensitive to this effect. At a width of 0.2 radians, the absolute value of ϵ decreased insignificantly in a few places, by no more than 0.05 from the original ϵ spectra.

Taking all of these error sources together, the total error (one standard deviation) in the β, γ, and ϵ angular distribution parameters is at most 0.5, including both random and systematic errors. Thus the error bars on our parameter values vary, but have a typical half width of 0.5. Near the peaks of the line shapes the repeatability of our β, γ, and ϵ parameter values (excluding systematic errors) was 0.2 or better. Due to the more complex data-taking and analysis procedures, these errors are significantly larger than the error on the β parameter of the 3*pns* Mg states [19]. The energy resolution of our spectra, determined by our laser linewidth, was about 1.0 cm^{-1}.

B. Discussion

In the previous work on the 3*pns* Mg angular distribution parameter [19], the β parameter was found to be relatively constant near $\beta \approx 2$, except for a few sharp dips to $\beta \approx -1$. That sort of structure is not seen in these 3*pnd* angular distribution spectra. Instead we measured parameter values, which vary irregularly. The fluctuations of the β parameter of the 3*pns* states were clearly correlated with the positions of interloping autoionizing states, which were not excited directly, but were at the same energies as the β parameter fluctuations. Although there are similar interloping resonances throughout the measured energy range of the 3*pnd* states, there is no obvious correlation between them and the features in the 3*pnd* angular distribution spectra. The 3*pnd* spectra are considerably more complex than the 3*pns* spectra, which is to be expected since the 3*pnd* states studied are more complex and have two angular momentum J manifolds.

As shown by Figs. 4, 5, and 6 the predicted β, γ, and ϵ spectra agree well with our measurements. Most of the small disagreement between experiment and theory can be explained by experimental error. The only significant systematic discrepancy is that the measured ϵ value is never more than about 2, whereas the theoretical value of ϵ reaches 3 at some energies. Since ϵ multiplies $P_6(\cos\theta)$, which varies most rapidly with θ, the ϵ parameter is most sensitive to systematic offsets in θ, and to the averaging of the angular distribution over θ. It is possible that we have underestimated the averaging of the angular distributions caused by the finite angular aperture of our electron detector. This would cause us to measure a smaller $|\epsilon|$ than the true $|\epsilon|$, but would have little effect on β and γ.

The different sorts of angular distributions observed are shown as polar plots in Fig. 7, along with the angular distribution of the 3*snd* ^1D level being photoionized. The expected propensity is that the photoelectron will be mainly ejected *along* the photon polarization axis. This is because the 3*snd* level is already elongated in that direction, and also because the photoionizing laser is applying an additional force on the electron cloud in that direction. If a low-lying 3*snd* level were being photoionized rather than a Rydberg level, one would argue [30,31] that the *nd* electron would be preferentially photoionized into the ϵf continuum rather than into the ϵp continuum. The classical argument is that in the course of absorbing energy and increasing in speed, the photoelectron is more likely to gain rather than lose angular momentum (a quantum version of this argument is given in Ref. [30]).

This simple argument needs to be modified to understand the present experiment, because it is really the 3*s* electron that is initially excited by the photoionizing laser, after which the 3*pnd* resonance levels decay by autoionization into the $3s\epsilon p$ and $3s\epsilon f$ continua. But a similar argument still applies in that the *nd* electron gains speed in the course of autoionizing and so has a propensity to gain angular momentum. For this reason the $3pnd \rightarrow 3s\epsilon f$ channel should be the dominant photoionization pathway. This propensity is verified by the relative $J=1$ and 3 contributions to the total photoionization cross section, shown in Figs. 4–6. The $J=3$ line shapes are much broader on average than $J=1$ line shapes since there is more of a propensity to autoionize to an f-wave continuum (the autoionization rate to f waves is faster). Therefore over most of the spectra, except near high and narrow $J=1$ resonances, the $J=3$ contribution is larger than the $J=1$ contribution.

Because a pure f-wave solution with $m_l=0$ is highly peaked along the quantization axis, this confirms that ejection along the polarization axis should be greatly favored (normally) over sideways photoejection near $\theta=\pi/2$. This propensity is verified in the angular distributions of the present experiment, with most energies

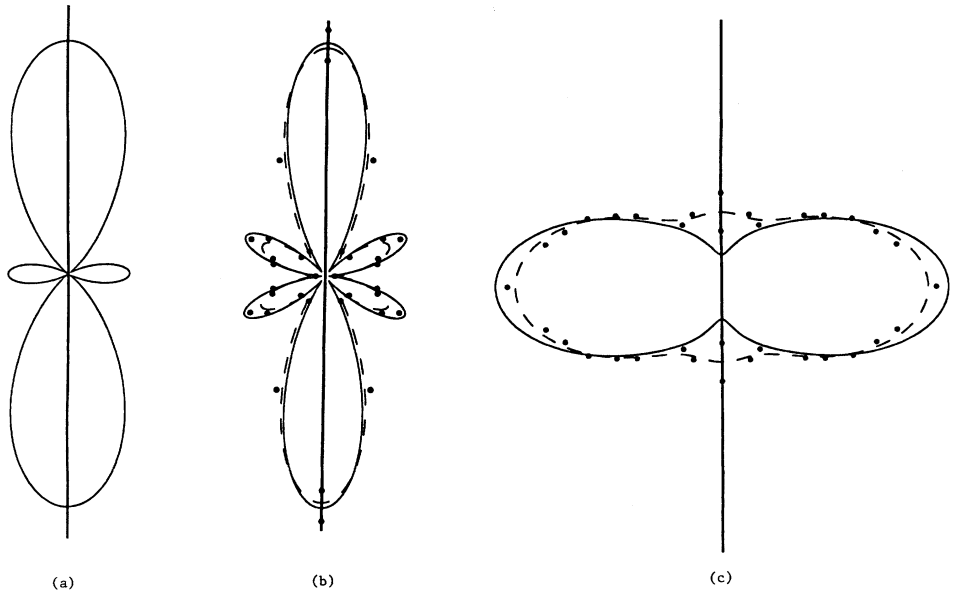

FIG. 7. (a) Angular distribution of the initial $|J_0\rangle$ $3snd$ state. $|\Psi|^2$ is proportional to $[P_2(\cos\theta)]^2$. (b) A typical "propensity favored" angular distribution. This is of the $3p18d$ state at 35 646 cm^{-1} above the $3s18d$ state. The solid line is the MQDT prediction for the angular distribution [of the form of Eq. (1a)]. The filled circles are the measurements of the normalized electron signal (differential cross section). $\theta=0$ is vertical on these polar plots. We measured $d\sigma/d\Omega$ only in the plane of the paper, and only on the interval [0°,90°]. The data have been copied onto the other three quadrants. The dashed line is a least-squares fit of the data to Eq. (1a). The parameters β, γ, and ε derived from the fit are the three data points of Fig. 6 at 35 646 cm^{-1}. The peak of $d\sigma/d\Omega$ along the quantization (laser polarization) axis is typical of photoionization. (c) A "propensity unfavored" angular distribution. This is of the $3p18d$ state at 35 687 cm^{-1} above the $3s18d$ state. This graph shows that at a few particular energies the electron can be ejected "sideways" due to the complex channel interactions.

displaying a photoelectron angular distribution peaked along the polarization vector, qualitatively similar to that shown in Fig. 7(b). Occasionally energies are probed, as in Fig. 7(c), which shows the propensity-unfavored case of predominantly sideways photoejection, but these tend to be comparatively rare.

A further complication to bear in mind when comparing the present theory and experiment is that the calculation has ignored all effects of hyperfine structure. For 90% of the Mg atoms, which have zero nuclear spin, this is exact. But for the remaining 10% having nuclear spin $I=\frac{5}{2}$, the hyperfine interaction causes **J** to precess about **F**, which can mix in the magnetic substates other than $M_J=0$. The validity of ignoring this precession depends on the relative time scales of hyperfine precession and of the laser excitation time. The precession periods are estimated to fall in the range of 10 to 25 ns for the Mg $3s3p\ ^1P^\circ$ state, which is slow though not entirely negligible compared to the 5 ns delay between absorption of the first and second laser photons. Since this affects only 10% of the atoms, however, this is likely to cause less than a 1–2% correction to the anisotropy parameters calculated in this study. The hyperfine precession appears to be negligible for *singlet* Rydberg states in the range studied here.

Equations (9a)–(9e), which form the angular distribution parameters, can be rewritten in terms of probabilities $P_{J_{cs}J}$, where $P_{J_{cs}J}$ represents the fraction of the total photoionization cross section contributed by states with J_{cs} and J. If $P_{J_{cs}J}$ is written as the square of a complex probability amplitude $|A_{J_{cs}J}|^2\equiv P_{J_{cs}J}$, then the $A_{J_{cs}J}$ are proportional to the $D_{J_{cs}J}$ of Eqs. (9). For example, $A_{01}=(\frac{2}{15})^{1/2}D_{01}/(a_0)^{1/2}$, etc. Then Eqs. (9b)–(9e) can be rewritten as

$$\beta=2P_{01}-P_{11}+\tfrac{4}{3}P_{03}+P_{13}-6(\tfrac{3}{7})^{1/2}\mathrm{Re}(A_{01}^{*}A_{03})-6(\tfrac{2}{7})^{1/2}\mathrm{Re}(A_{11}^{*}A_{13})\ , \tag{23a}$$

$$\gamma=\tfrac{18}{11}P_{03}+\tfrac{3}{11}P_{13}-8(\tfrac{3}{7})^{1/2}\mathrm{Re}(A_{01}^{*}A_{03})+6(\tfrac{2}{7})^{1/2}\mathrm{Re}(A_{11}^{*}A_{13})\ . \tag{23b}$$

$$\epsilon=\tfrac{100}{33}P_{03}-\tfrac{75}{33}P_{13}\ . \tag{23c}$$

The P's must be in the range [0,1], and the A's must have a magnitude less than or equal to 1. Also the sum $P_{01}+P_{11}+P_{03}+P_{13}$ must equal 1 for all cases. These constraints allow one to determine the maximum and minimum values of the parameters. ϵ clearly lies in the range $[-2.27,3.03]$. A Monte Carlo calculation using all possible values of the A's shows that β is in the range $[-1.86,3.65]$, and γ is in the range $[-1.92,3.56]$. These limits agree very well with our measurements, and agree perfectly with our theoretical results. The excursions of our measured parameters past these limiting values are due to noise in the data.

In order to understand the forms of the β, γ, and ϵ parameter spectra, we shall discuss the contributions to the

theoretical parameter spectra. As shown by Eq. (9) the terms that form β, γ, and ϵ can be divided into three categories. The pure $J=1$ terms contain only matrix elements of the form $|D_{J_{cs}1}|^2$. The pure $J=3$ terms contain only elements of the form $|D_{J_{cs}3}|^2$. The "mixed J" terms are of the form $\mathrm{Re}(D^*_{J_{cs}1}D_{J_{cs}3})$. The a_0 parameter contains pure $J=1$ and 3 terms but no mixed J terms. a_2 contains all three types of terms. a_4 contains no pure $J=1$ terms, and a_6 contains only pure $J=3$ terms. Thus β and γ contain mixed J terms, while ϵ does not. This is since in the calculation of a_k, as k increases, more and more of the terms in the summation of Eq. (8b) are zero, due to the triangle rule for the $3j$ symbol $\begin{pmatrix} k & J' & J \\ 0 & 0 & 0 \end{pmatrix}$, with J and J' never more than 3.

We can separate the contributions of the three categories of matrix element products to the theoretical β spectrum of the $3p\,12d$ state, as shown in Fig. 8. The top line of Fig. 8 shows the pure $J=1$ contributions to β. In other words, the top line is a graph of

$$\frac{\frac{2}{15}(2|D_{01}|^2-|D_{11}|^2}{a_0} .$$

The line labeled $J=3$ shows the pure $J=3$ contribution to β; it is a graph of

$$\frac{\frac{1}{35}(4|D_{03}|^2+3|D_{13}|^2)}{a_0} .$$

The line labeled mixed J is a graph of

$$\frac{-\frac{6}{35}[\sqrt{6}\,\mathrm{Re}(D^*_{01}D_{03})+2\,\mathrm{Re}(D^*_{11}D_{13})]}{a_0} ,$$

the mixed J contribution to β. In each case the full a_0 of Eq. (9a) is used, so that the sum of the three partial β parameters is the total β. This means the $J=3$ line, for example, still has some $J=1$ contribution coming from a_0 in the denominator.

Figure 9 shows the same arrangement for the theoretical γ parameter of the $3p\,12d$ state. Since a_4 has no pure $J=1$ terms, the top line of Fig. 8 is missing from Fig. 9 (ϵ has only pure $J=3$ terms, so it cannot be divided up in the same way as β and γ).

Figures 8 and 9 show clearly that the structure of the β and γ parameters is overwhelmingly due to the mixed J terms of the a_2 and a_4 parameters. The shapes of the total β and total γ graphs are quite similar to the mixed J term graphs. The pure $J=1$ and $J=3$ term graphs tend to fluctuate as a function of energy much less than do the

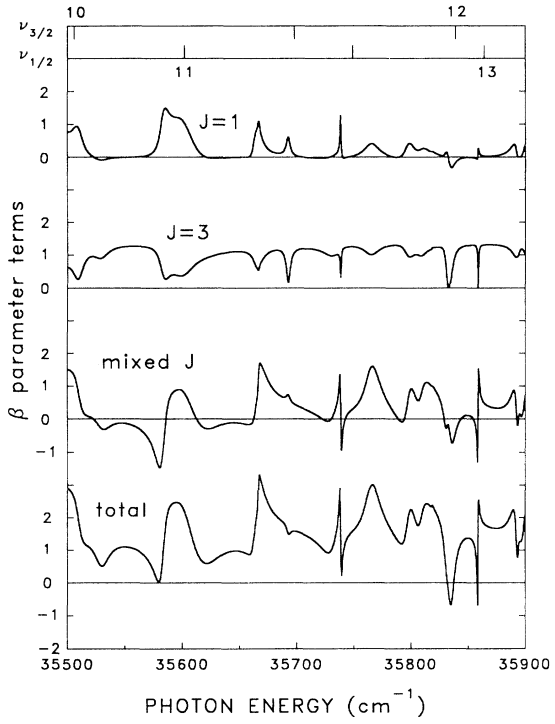

FIG. 8. Various contributions to the β parameter spectrum of the $3p\,12d$ state of Mg. In order from top to bottom, the graphs are of the $\beta=a_2/a_0$ parameter with a_2 consisting only of pure $J=1$ terms, only of pure $J=3$ terms, and only of mixed J terms. In all cases the a_0 used is the full a_0 of Eq. (9a). The bottom line is the complete β parameter, which is the sum of the top three graphs. This figure is purely theoretical. As in Figs. 4–6 the solid horizontal lines indicate the zeros of the parameters. As discussed in the text the mixed J terms provide the major contribution to the total β parameter shape.

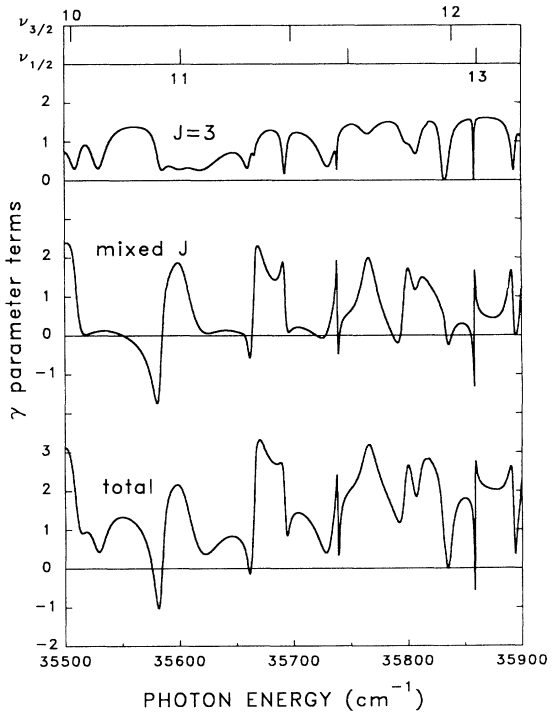

FIG. 9. Similar to Fig. 8, this figure shows the various contributions to the γ parameter spectrum of the $3p\,12d$ state of Mg. In order from top to bottom, the graphs are of the $\gamma=a_4/a_0$ parameter with a_4 consisting only of pure $J=3$ terms, then only of mixed J terms, and on the bottom the sum of the top two, which is the full γ parameter. The a_0 used is the full a_0 of Eq. (9a). The γ parameter has no pure $J=1$ terms. As with the β parameter, the mixed J terms provide the major contribution to the total γ parameter shape.

mixed J term graphs and so they contribute less to the shape of the total β and γ parameters. The pure $J=1$ and 3 terms do contribute significantly to the numerical values of the β and γ parameters.

In Figs. 4–6 there appears to be a pattern of sharp shifts, peaks, or dips near the peaks of the line shape. The peaks of the transition line shapes are mostly due to very narrow $J=1$ features in the spectra. As shown in the total-cross-section traces in Figs. 4–6 and in Ref. [3], the line-shape signal due to $J=1$ $3pnd$ states has only very narrow and high peaks, with almost no signal between the peaks. The $J=3$ $3pnd$ line shape is more slowly varying with energy and has broad peaks that overlap each other. An angular distribution can be derived from the $J=1$ states only and from the $J=3$ states only; each is different. Over most of the energy range the $J=3$ line shape predominates; so the total angular distribution parameters mostly reflect the $J=3$ distribution. Only at the narrow peaks of the line shape would the separate $J=1$ distribution predominate; there, the total angular distribution would reflect the $J=1$ distribution. The ϵ parameter shows the clearest distinction between $J=1$ and $J=3$ contributions. The ϵ parameter has a $J=1$ contribution only via the a_0 denominator. A pure $J=3$ ϵ parameter can be written by eliminating the $J=1$ portion of a_0. This altered ϵ is given as

$$\epsilon^{J=3}=\frac{\frac{5}{77}(4|D_{03}|^2-3|D_{13}|^2)}{\frac{3}{35}(|D_{03}|^2+|D_{13}|^2)} .$$

$\epsilon^{J=3}$ has a graph similar to the unaltered ϵ, as shown in Fig. 10, however $\epsilon^{J=3}$ has no sharp dips interspersed among the broad fluctuations. These sharp dips, and the other features of the parameters that vary rapidly with energy, are due to the $J=1$ contributions. Examples of these $J=1$ features are the parameters of $3p12d$ at 35 690 and 35 860 cm^{-1}, and of $3p10d$ at 35 635 cm^{-1}.

Relatively weak and narrow features due to g states can be seen in the measured and theoretical spectra, e.g., in the $3p12d$ angular distribution of Fig. 5 at 35 668 cm^{-1}. These must be due to $J=3$ $3png$ states since the features do not appear in the theoretical calculations which exclude g states, shown as dotted lines in Figs. 4–6.

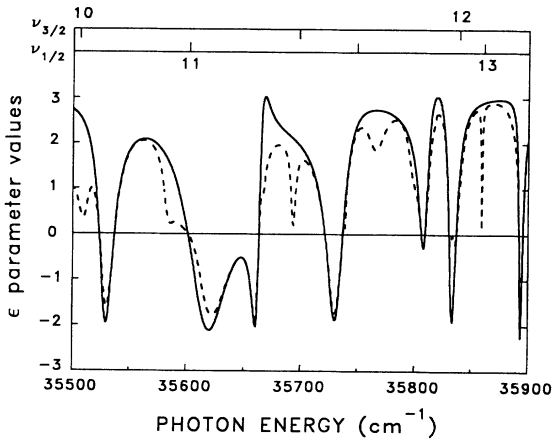

FIG. 10. Solid line is the ϵ parameter with all of the $J=1$ terms removed from it, both from the numerator and from the a_0 denominator. This is called $\epsilon^{J=3}$ in the text. Also shown is the unaltered true ϵ parameter as a dotted line. The lack of sharp dips in the altered $\epsilon^{J=3}$ parameter shows that the dips and very rapid variation in the actual parameters are due to the $J=1$ contribution.

V. CONCLUSION

We have measured the angular distributions of autoionized electrons ejected from $3pnd$ $J=1$ and $J=3$ states of Mg and have obtained their angular distribution parameter spectra over the range of n from 10 to 18. The measured spectra are complex and irregular. They appear drastically different from the $3pns$ $J=1$ angular distribution parameter spectra measured previously [19]. We have also calculated the angular distribution parameter spectra using $\underline{K}$ matrices and an MQDT formalism. The calculated $3pnd$ spectra agree well with the measured $3pnd$ spectra, to within experimental error.

We find that the different J states *can* produce interference in the emitted electron spectra, but only in some (β and γ) angular distribution parameter spectra. In the ϵ parameter spectra and in the total cross section σ, the different J states do not interfere.

The line-shape measurements of Mg autoionizing states reported in Refs. [2] and [3], the angular distribution measurements in Ref. [19] of the Mg $3pns$ $J=1$ states, and the angular distribution measurements of the Mg $3pnd$ $J=1$ and 3 states described in this paper form a progression of measurements that involve successively more and more complex sets of channels and wave functions. The quantities measured represent successively more and more stringent tests of the $\underline{K}$ matrices and of the R-matrix approach itself. The less stringent test described in Refs. [2] and [3] results in quite good agreement between theory and experiment. The test of intermediate stringency, involving the angular distribution of the relatively simple $3pns$ $J=1$ states excited by one photon from a spherically symmetric $J=0$ state, shows good agreement, but there are a few significant discrepancies [19]. This paper measures the angular distributions of the fairly complex $3pnd$ states with relatively high angular momentum, and for these states the $\underline{K}$ matrices also match well with the measurements.

ACKNOWLEDGMENT

This work has been supported by the U.S. Department of Energy, Office of Basic Energy Sciences.

APPENDIX

This appendix contains an alternate means of calculating the reduced matrix elements $D_{J_{cs}J}$ of Eq. (22). This formulation can replace Eqs. (10)–(22), and was derived independently. As can be seen in Figs. 4–6, the results of each formulation are essentially the same, serving as a check on the validity of both.

The final dissociation states, in which the electrons are far apart, are most naturally described by jj coupling, so in this formulation we work in the jj coupled scheme, converting the $\underline{K}$ matrix to jj coupling. (In all of the fol-

lowing the trailing superscript of any quantity refers to its corresponding J, i.e., ϕ^1 means $\phi^{J=1}$.) We use seven $J=1$ channels and five $J=3$ channels. They are listed in jj and LS coupling as follows:

$$\begin{bmatrix}\phi_1^1\\ \phi_2^1\\ \phi_3^1\\ \phi_4^1\\ \phi_5^1\\ \phi_6^1\\ \phi_7^1\end{bmatrix} = \begin{bmatrix}3s_{1/2}\epsilon p_{1/2}\\ 3s_{1/2}\epsilon p_{3/2}\\ 3p_{1/2}ns_{1/2}\\ 3p_{3/2}ns_{1/2}\\ 3p_{1/2}nd_{3/2}\\ 3p_{3/2}nd_{3/2}\\ 3p_{3/2}nd_{5/2}\end{bmatrix} = \underline{V}^1 \begin{bmatrix}\psi_1^1\\ \psi_2^1\\ \psi_3^1\\ \psi_4^1\\ \psi_5^1\\ \psi_6^1\\ \psi_7^1\end{bmatrix} = \underline{V}^1 \begin{bmatrix}3s\epsilon p\ ^1P_1\\ 3pns\ ^1P_1\\ 3pnd\ ^1P_1\\ 3s\epsilon p\ ^3P_1\\ 3pns\ ^3P_1\\ 3pnd\ ^3P_1\\ 3pnd\ ^3D_1\end{bmatrix} \tag{A1}$$

and

$$\begin{bmatrix}\phi_1^3\\ \phi_2^3\\ \phi_3^3\\ \phi_4^3\\ \phi_5^3\end{bmatrix} = \begin{bmatrix}3s_{1/2}\epsilon f_{5/2}\\ 3s_{1/2}\epsilon f_{7/2}\\ 3p_{1/2}nd_{5/2}\\ 3p_{3/2}nd_{3/2}\\ 3p_{3/2}nd_{5/2}\end{bmatrix} = \underline{V}^3 \begin{bmatrix}\psi_1^3\\ \psi_2^3\\ \psi_3^3\\ \psi_4^3\\ \psi_5^3\end{bmatrix} = \underline{V}^3 \begin{bmatrix}3pnd\ ^3D_3\\ 3s\epsilon f\ ^1F_3\\ 3pnd\ ^1F_3\\ 3s\epsilon f\ ^3F_3\\ 3pnd\ ^3F_3\end{bmatrix} . \tag{A2}$$

The orthogonal matrices $\underline{V}^1$ and $\underline{V}^3$ are given in Refs. [19] and [2], respectively. For this alternate derivation of the $D_{J_{cs}J}$ we use the older $\underline{K}$ matrices of Ref. [2] ($J=1$) and Ref. [3] ($J=3$). These were calculated with a box size of $r_0=12$ a.u., and do not include $3png$ states. As described in detail in Ref. [19], those $\underline{K}$ matrices allow us to calculate the channel amplitudes $A^J_{i\rho}$, where

$$\Psi^J_\rho = \sum_i A^J_{i\rho}\phi^J_i . \tag{A3}$$

Ψ_ρ is the collision eigenstate of the system after ionization. For each J there are two open channels, and so two collision eigenstates that are labeled by $\rho=1,2$. The Ψ^J_ρ are linear combinations of the jj coupled channels. Via the procedures described in detail in Ref. [19] we also obtain the phase shifts τ^J_ρ of the open-channel continuum wave functions from the $\underline{K}$ matrices.

Since our reduced matrix element kets $|[J_c s)J_{cs}l]J-\rangle$ are in J_cJ_{cs} coupling, which in this case is equivalent to LS coupling, since for our final states $J_{cs}=S$ and $l=L$, we must also convert them to jj coupling before using them. This can be done using submatrices of the $\underline{V}^J$'s of Eqs. (A1) and (A2). In particular, we will need

$$\begin{bmatrix}|[J_{cs}=0l=1]J=1\rangle\\ |[J_{cs}=1l=1]J=1\rangle\end{bmatrix} = \begin{bmatrix}3s\epsilon p\ ^1P_1\\ 3s\epsilon p\ ^3P_1\end{bmatrix} = \begin{bmatrix}W^1_{11} & W^1_{12}\\ W^1_{21} & W^1_{22}\end{bmatrix}\begin{bmatrix}\phi^1_1\\ \phi^1_2\end{bmatrix} = \begin{bmatrix}(\frac{1}{3})^{1/2} & (\frac{2}{3})^{1/2}\\ (\frac{2}{3})^{1/2} & -(\frac{1}{3})^{1/2}\end{bmatrix}\begin{bmatrix}3s_{1/2}\epsilon p_{1/2}\\ 3s_{1/2}\epsilon p_{3/2}\end{bmatrix} \tag{A4}$$

and

$$\begin{bmatrix}|[J_{cs}=0l=3]J=3\rangle\\ |[J_{cs}=1l=3]J=3\rangle\end{bmatrix} = \begin{bmatrix}3s\epsilon f\ ^1F_3\\ 3s\epsilon f\ ^3F_3\end{bmatrix} = \begin{bmatrix}W^3_{11} & W^3_{12}\\ W^3_{21} & W^3_{22}\end{bmatrix}\begin{bmatrix}\phi^3_1\\ \phi^3_2\end{bmatrix} = \begin{bmatrix}(\frac{3}{7})^{1/2} & (\frac{4}{7})^{1/2}\\ (\frac{4}{7})^{1/2} & -(\frac{3}{7})^{1/2}\end{bmatrix}\begin{bmatrix}3s_{1/2}\epsilon f_{5/2}\\ 3s_{1/2}\epsilon f_{7/2}\end{bmatrix} . \tag{A5}$$

The $\underline{W}^J$ matrices are simply subblocks of the $\underline{V}^J$ matrices corresponding to the open channels.

We may now write the reduced matrix elements $D_{J_{cs}J}$ as

$$\begin{aligned} D_{01} = \langle [(J_c s)J_{cs}=0l]J=1-\|r^{(1)}\|J_0\rangle &= \sum_{i=1}^{2} W^1_{1i}\langle \phi^1_i-\|r^{(1)}\|J_0\rangle \\ &= \sum_{i=1}^{2} W^1_{1i}\sum_{\rho=1}^{2}\langle \phi^1_i|\Psi^1_\rho\rangle\langle \Psi^1_\rho-\|r^{(1)}\|J_0\rangle \\ &= \sum_{i=1}^{2}\sum_{\rho=1}^{2} W^1_{1i}\sum_{j=1}^{7}\langle \phi^1_i|\phi^1_j\rangle A^1_{j\rho}\sum_{k=1}^{7} A^1_{k\rho}\langle \phi^1_k-\|r^{(1)}\|J_0\rangle \\ &= \sum_{i=1}^{2}\sum_{\rho=1}^{2} W^1_{1i}A^1_{i\rho}\sum_{k=5}^{7} A^1_{k\rho}\langle \phi^1_k-\|r^{(1)}\|J_0\rangle \\ &= \sum_{i=1}^{2}\sum_{\rho=1}^{2}\sum_{k=5}^{7} W^1_{1i}A^1_{i\rho}A^1_{k\rho}M^1_{k\rho} , \end{aligned} \tag{A6a}$$

using $\sum_\rho |\Psi_\rho^J\rangle\langle\Psi_\rho^J|$ and $|J_0\rangle = |3snd\ ^1D_2\rangle$. Here $M_{k\rho}^J \equiv \langle \phi_k^J - \|r^{(1)}\| J_0\rangle$. Similarly,

$$D_{11} = \sum_{i=1}^{2}\sum_{\rho=1}^{2}\sum_{k=5}^{7} W_{2i}^1 A_{i\rho}^1 A_{k\rho}^1 M_{k\rho}^1 , \tag{A6b}$$

$$D_{03} = \sum_{i=1}^{2}\sum_{\rho=1}^{2}\sum_{k=3}^{5} W_{1i}^3 A_{i\rho}^3 A_{k\rho}^3 M_{k\rho}^3 , \tag{A6c}$$

$$D_{13} = \sum_{i=1}^{2}\sum_{\rho=1}^{2}\sum_{k=3}^{5} W_{2i}^3 A_{i\rho}^3 A_{k\rho}^3 M_{k\rho}^3 . \tag{A6d}$$

Reading from right to left, the factors in the last form of Eq. (A6) can be understood as follows: $M_{k\rho}^J$ is the dipole matrix element connecting the bound initial $3snd$ state to the kth closed channel. $A_{k\rho}^J$ is the amplitude of the kth channel in the ρth eigenchannel. Summing $A_{k\rho}^J M_{k\rho}^J$ over k gives the amplitude for excitation of the ρth eigenchannel. $A_{i\rho}^J$ is the amplitude of the ith open channel in the ρth eigenchannel, and is thus the fractional amplitude for decay into the ith open channel. Finally W_{1i}^J gives the fraction of the ith channel that is singlet, and W_{2i}^J gives the fraction that is triplet. When all the factors are put together the $D_{J_{cs}J}$ matrix element is the amplitude for the transition from the initial $3snd$ state to the J_{cs}, J continuum.

The states $|\phi_k^J\rangle$ listed in Eqs. (A1) and (A2), with $k=5,6,7$, for $J=1$ and $k=3,4,5$ for $J=3$ will be written now as $|3p_{J_c'}\nu' d\rangle$, where ν' is the effective principal quantum number of the outer electron's state. ν' is not necessarily an integer. ν' is determined by the ionization potential $E_{J_c'}$ with respect to the excited ion core. (J_c' is the total angular momentum of the excited ion core.) ν' of a state with J_c' is given by

$$\nu' = \left[\frac{R}{E_{J_c'} - E}\right]^{1/2} , \tag{A7a}$$

where R is the Rydberg constant for Mg: 109 734.86 cm^{-1}. E in Eq. (A7a) is the total energy of the autoionizing state. $E_{3p1/2}$ is 97 340.33 cm^{-1} and $E_{3p3/2}$ is 97 431.90 cm^{-1}. When rewriting the initial state $|J_0\rangle$,

$$\nu = \left[\frac{R}{E_{3s} - E}\right]^{1/2} , \tag{A7b}$$

where E_{3s} is the normal ionization potential of Mg with an unexcited core 61 671.02 cm^{-1} and E in Eq. (A7b) is the energy of the $|J_0\rangle$ state [22]. Note that $|J_0\rangle$ in jj coupling is $(\frac{2}{5})^{1/2}|3s_{1/2}\nu d_{3/2}\rangle + (\frac{3}{5})^{1/2}|3s_{1/2}\nu d_{5/2}\rangle$. The transformation coefficients here and in the $\underline{V}$ and $\underline{W}$ matrices come from Eq. 6.4.16 of Ref. [27].

We must now calculate the $M_{k\rho}^J$. They can be written as a product of a radial integral, an angular integral, an overlap integral, and a phase factor:

$$M_{k\rho}^J = \langle \phi_k^J \| rC^{(1)} \| J_0\rangle \langle \nu_k' | \nu\rangle \exp(i\pi\tau_\rho^J) i^{-l} \exp(i\sigma_l) . \tag{A8}$$

$\langle \nu_k' | \nu\rangle$ is given in Ref. [32] as

$$\langle \nu_k' | \nu\rangle = \frac{2(\nu\nu_k')^2 \sin\pi(\nu_k' - \nu)}{\nu^{3/2}\pi(\nu_k'^2 - \nu^2)} . \tag{A9}$$

ν_k' is the $\nu_{J_c'}'$ with the J_c' of the corresponding $|\phi_k^J\rangle$. In the first exponential of Eq. (A8), the τ_ρ^J comes from the $\underline{K}^J$ matrices, as described in Ref. [19]. $i^{-l}\exp(i\sigma_l)$ is the Coulomb phase factor, in which l is the orbital angular momentum of the outgoing electron. This is 1 or 3 in our case. $\sigma_l = \arg\Gamma(l+1-i/k)$, where $k^2/2$ is the kinetic energy of the free electron; i.e., $k^2/2 = E - E_{3s}$, in atomic units. $C^{(1)}$ is the first-rank renormalized spherical harmonic tensor operator [28], such that $\mathbf{r}^{(1)} = rC^{(1)}$. We have evaluated its matrix elements in jj coupling using Eq. 7.1.7 of Ref. [27] twice, which leads to the formula

$$\begin{aligned}\langle (l_1' s_1') j_1' (l_2' s_2') j_2' J' \| rC^{(k=1)} \| (l_1 s_1) j_1 (l_2 s_2) j_2 J\rangle \\ = X_r (-1)^{J+j_1+j_2+j_1'+s_1} [J][J'][j_1][j_1'][l_1'][l_1] \\ \times \begin{Bmatrix} l_1' & k & l_1 \\ 0 & 0 & 0 \end{Bmatrix} \begin{Bmatrix} j_1' & J' & j_2 \\ J & j_1 & k \end{Bmatrix} \begin{Bmatrix} l_1' & j_1' & s_1 \\ j_1 & l_1 & k \end{Bmatrix} ,\end{aligned} \tag{A10}$$

where X_r is the radial integral. Since X_r is common to all of the $M_{k\rho}^J$, we ignore it from now on. (Here we make the good approximation that the radial integrals are equal for $3p_{1/2}$ and $3p_{3/2}$ states.) We find the $M_{k\rho}^J$ as shown in Table V.

To summarize this derivation, the $M_{k\rho}^J$, which are complex numbers, go into the summations of Eq. (A6), producing the reduced matrix elements $D_{J_{cs}J}$, which are also complex numbers. Equation (9) uses these matrix elements to calculate the real angular distribution parameters β, γ, and ϵ as a function of energy. The $\underline{K}$ matrices

TABLE V. The reduced matrix elements $M_{k\rho}^J$ used in calculation of the angular distribution parameters of the $3pnd$ states of Mg. We have evaluated the $\arg\Gamma(l+1-i/k)$ in the Coulomb phase using Eqs. 6.1.15 and 6.1.24 of Ref. [33]. In this table we have excluded a common factor of $\exp(i\{\arg[(-i/k)\Gamma(-i/k)] + \tan^{-1}(-1/k)\})$ (and the radial integral) from all of the M's.

$M_{5\rho}^1$	$+(\frac{1}{3})^{1/2}\langle \nu_{1/2}' \| \nu\rangle \exp(i\pi\tau_\rho^1)(-i)$
$M_{6\rho}^1$	$+(\frac{1}{15})^{1/2}\langle \nu_{3/2}' \| \nu\rangle \exp(i\pi\tau_\rho^1)(-i)$
$M_{7\rho}^1$	$+(\frac{3}{5})^{1/2}\langle \nu_{3/2}' \| \nu\rangle \exp(i\pi\tau_\rho^1)(-i)$
$M_{3\rho}^3$	$-(\frac{7}{9})^{1/2}\langle \nu_{1/2}' \| \nu\rangle \exp(i\pi\tau_\rho^3)(+i)\exp\{i[\tan^{-1}(-1/2k) + \tan^{-1}(-1/3k)]\}$
$M_{4\rho}^3$	$+(\frac{14}{15})^{1/2}\langle \nu_{3/2}' \| \nu\rangle \exp(i\pi\tau_\rho^3)(+i)\exp\{i[\tan^{-1}(-1/2k) + \tan^{-1}(-1/3k)]\}$
$M_{5\rho}^3$	$+(\frac{28}{45})^{1/2}\langle \nu_{3/2}' \| \nu\rangle \exp(i\pi\tau_\rho^3)(+i)\exp\{i[\tan^{-1}(-1/2k) + \tan^{-1}(-1/3k)]\}$

are slowly varying functions of energy; the energy dependence of β, γ, and ϵ comes primarily from the calculation of ν' and the rapidly varying phases τ_ρ^J.

The difference between theoretical parameters calculated in this appendix and the parameters calculated in Sec. III, is that here we use an earlier version of the $\underline{K}$ matrices (the same as those used in Refs. [2,3,19], which are less accurate and also neglect the 3*png* $J=3$ channels. Although the MQDT analyses here and in Sec. III are quite different, they produce the same parameter values if the input $\underline{K}$ matrices are the same. The differences shown in Figs. 4, 5, and 6 between the theoretical methods indicates the errors in the less precise $\underline{K}$ matrices used in this appendix and in Refs. [2,3,19].

[1] M. J. Seaton, Rep. Prog. Phys. **46**, 167 (1983); C. H. Greene, Phys. Rev. A **28**, 2209 (1983); J. Opt. Soc. Am. B **4**, 775 (1987).

[2] C. J. Dai, G. W. Schinn, and T. F. Gallagher, Phys. Rev. A **42**, 223 (1990).

[3] G. W. Schinn, C. J. Dai, and T. F. Gallagher, Phys. Rev. A **43**, 2316 (1991).

[4] L. Kim and C. H. Greene, Phys. Rev. A **36**, 4272 (1987).

[5] V. Lange, U. Eichmann, and W. Sandner, J. Phys. B **22**, L245 (1989).

[6] M. Aymar, J. Phys. B **20**, 6507 (1987).

[7] E. Y. Xu, Y. Zhu, O. C. Mullins, and T. F. Gallagher, Phys. Rev. A **33**, 2401 (1986).

[8] M. Aymar and J. M. Lecomte, J. Phys. B **22**, 223 (1989).

[9] C. J. Dai, S. M. Jaffe, and T. F. Gallagher, J. Opt. Soc. Am. B **6**, 1486 (1989).

[10] V. Lange, M. Aymar, U. Eichmann, and W. Sandner, J. Phys. B **24**, 91 (1991).

[11] H. Hieronymus, M. Kohl, J. Neukammer, A. König, H. Rinneberg, and H. Spinger-Bolk, Phys. Rev. A **41**, 1477 (1990).

[12] R. Kachru, N. H. Tran, P. Pillet, and T. F. Gallagher, Phys. Rev. A **31**, 218 (1985).

[13] O. C. Mullins, R. Chien, J. E. Hunter, D. K. Jordan, and R. S. Berry, Phys. Rev. A **31**, 3059 (1985).

[14] O. C. Mullins, J. E. Hunter, J. S. Keller, and R. S. Berry, Phys. Rev. Lett. **54**, 410 (1985).

[15] O. C. Mullins, R. Chien, J. E. Hunter, J. S. Keller, and R. S. Berry, Phys. Rev. A **31**, 321 (1985).

[16] G. Leuchs and S. J. Smith, Phys. Rev. A **31**, 2283 (1985).

[17] E. Matthias, P. Zoller, D. S. Elliot, N. D. Piltch, S. J. Smith, and G. Leuchs, Phys. Rev. Lett. **50**, 1914 (1983).

[18] Y. Zhu, E. Y. Xu, and T. F. Gallagher, Phys. Rev. A **36**, 3751 (1987).

[19] M. D. Lindsay, L.-T. Cai, G. W. Schinn, C.-J. Dai, and T. F. Gallagher, Phys. Rev. A **45**, 231 (1992).

[20] S. J. Smith and G. Leuchs, in *Advances in Atomic and Molecular Physics,* edited by D. Bates and B. Bederson (Academic, New York, 1988), Vol. 24, pp. 157–221.

[21] *Atomic Excitation and Recombination in External Fields,* edited by M. H. Nayfeh and C. W. Clark (Gordon and Breach, New York, 1985); *Electronic and Atomic Collisions: Invited Papers,* edited by J. Eichler *et al.* (North-Holland, New York, 1984).

[22] W. C. Martin, and R. Zalubas, J. Phys. Chem. Ref. Data **9**, 4 (1980).

[23] T. F. Gallagher, J. Opt. Soc. Am. B **4**, 794 (1987).

[24] M. I. T. Wavelength Tables, edited by F. M. Phelps (MIT, Cambridge, MA, 1982), Vol. 2. p. 3.

[25] W. H. Press, B. P. Flannery, S. A. Teukolsky, and W. T. Vetterling, *Numerical Recipes: The Art of Scientific Computing* (Cambridge University Press, New York, 1986), p. 518ff.

[26] M. Weissbluth, *Atoms and Molecules* (Academic, New York, 1978), pp. 11 and 12.

[27] A. R. Edmonds, *Angular Momentum in Quantum Mechanics* (Princeton University Press, Princeton, NJ, 1960).

[28] R. D. Cowan, *The Theory of Atomic Structure and Spectra* (University of California Press, Berkeley, 1981), pp. 306 and 307.

[29] A. F. Starace, in *Handbuch der Physik,* edited by W. Mehlhorn (Springer-Verlag, Berlin, 1982), Vol. 31.

[30] U. Fano, Phys. Rev. A **32**, 617 (1985).

[31] C. H. Greene, in *Fundamental Processes of Atomic Dynamics,* edited by J. S. Briggs *et al.* (Plenum, New York, 1988), p. 177.

[32] S. A. Bhatti, C. L. Cromer, and W. E. Cooke, Phys. Rev. A **24**, 161 (1981).

[33] *Handbook of Mathematical Functions,* edited by M. Abramowitz and I. A. Stegun (Dover, New York, 1972).